# EXPLORATIONS OF FUNCTIONALIZED GOLD NANOPARTICLE SURFACE CHEMISTRY FOR LASER DESORPTION IONIZATION MASS SPECTROMETRY APPLICATIONS

A Thesis

by

MARIO ESTUARDO GOMEZ HERNANDEZ

Submitted to the Office of Graduate Studies
Texas A&M University
in partial fulfillment of the requirements for the degree of

MASTER OF SCIENCE

May 2011

Major Subject: Chemistry

# EXPLORATIONS OF FUNCTIONALIZED GOLD NANOPARTICLE SURFACE CHEMISTRY FOR LASER DESORPTION IONIZATION MASS SPECTROMETRY APPLICATIONS

A Thesis

by

MARIO ESTUARDO GOMEZ HERNANDEZ

Submitted to the Office of Graduate Studies of
Texas A&M University
in partial fulfillment of the requirements for the degree of

MASTER OF SCIENCE

Approved by:

| | |
|---|---|
| Chair of Committee, | David H. Russell |
| Committee Members, | Paul S. Cremer |
| | Emile Schweikert |
| | Andreas Holzenburg |
| Head of Department, | David H. Russell |

May 2011

Major Subject: Chemistry

ABSTRACT

Explorations of Functionalized Gold Nanoparticle Surface Chemistry for

Laser Desorption Ionization Mass Spectrometry Applications. (May 2011)

Mario Estuardo Gomez Hernandez, B.S., Texas A&M University-Kingsville;

M.S., Texas A&M University-Kingsville

Chair of Advisory Committee: Dr. David H. Russell

Functionalized nanoparticles provide a wide range of potential applications for Biological Mass Spectrometry (MS). Particularly, we have studied the effects of chromophore activity on the performance of gold nanoparticles (AuNPs) capped with substituted azo (-N=N-) dyes for analyte ion production in Laser Desorption Ionization Mass Spectrometry (LDI-MS) conditions. A series of aromatic thiol compounds were used as Self-Assembled Monolayers (SAM) to functionalize the surface of the AuNPs. Results indicate that AuNPs functionalized with molecules having an active azo chromophore provide enhanced analyte ion yields than the nanoparticles capped with the hydrazino analogs or simple substituted aromatic thiols.

We have also conducted experiments using the azo SAM molecules on 2, 5, 20, 30, and 50 nm AuNPs exploring the changes of Relative Ion Yield (RIY) with increased AuNP diameters. Our results indicate that the role of the SAM to drive energy deposition decreases as the size of the AuNP increases. It was determined that 5 nm is the optimum size to exploit the benefits of the SAM on the ionization and selectivity of the AuNPs.

# DEDICATION

***To God the Father from whom all blessings flow***
***To Jesus Christ, Master and Essence of existence***
***To the Holy Spirit, Parakletos,***
***Thank you for counting me***
***as worthy of your grace,***
***taking my place on the cross,***
***dying my deserved death,***
***bringing me to life,***
***Even though I was not…***

***To my parents Hugo and Miriam***
***for believing in a dream and***
***doing everything in their power to***
***help me see it come true…***
***To my Siblings Hugo, Gabriel, and Christa***
***for bringing joy into growing up…***

***To my grandparents Mario, Maria del Rosario,***
***Ruth Estela and Eliseo (RIP) for their love***
***and support.***

***To the State of Texas, for providing me the funds***
***to attend Texas A&M University.***

***To the faculty and staff at the***
***Department of Chemistry***
***for being more than a department,***
***for being a family…***

***To my home country, Guatemala,***
***its people and its future…***

# ACKNOWLEDGMENTS

There is an old saying that goes: “Every 10,000 miles trip starts with one single step” For me, such a voyage started in the fall of 2006. In acknowledging the people that have made a contribution to my development, I would like to start by expressing my gratitude to my advisor Dr. David H. Russell, for his constant guidance to make me a better scientist and a better thinker. I will always be grateful. I also want to thank each of the professors at the Department of Chemistry under whom I have received lectures and training. I believe I came to the right place to receive advanced chemistry training. Nowhere else could I have had such personal input from world class faculty into my development as a student and scientist. I also want to thank the members of my graduate committee, Dr. Paul Cremer, Dr, Emile Schweikert, and Dr. Andreas Holzenburg for their dedication to guide and help newer generations of scientists around the world.

I also want to thank past and present members of the Russell research laboratory for their friendship and support through the challenges of graduate school. In addition, I want to thank Dr. Edward T. Castellana, for his constant help and friendship not only in experimental and scientific issues, but also in life issues in general. I also want to thank Dr. William K. Russell for always having time to listen to my questions, and for giving me career advice during my mass spectrometry training. Having a great group of people around during graduate school is essential to reaching goals and milestones in my career. I also want to thank Dr. Brian Connell and his student Alejandro Bugarin for allowing me access to their organic synthesis equipment for the purification and storage of my azo dyes. I also want to acknowledge the staff at the Microscopy and Imaging Center at

Texas A&M especially Dr. Zhipping Luo for training me in using the JEOL 2010 Transmission Electron Microscope to conduct the characterization of my gold nano particles.

Four years ago, I left Mom and Dad, four years ago I believed in a dream, a promise, and took a leap of faith. I am so convinced that I made the right choice, but this happy ending would not been possible without the support, effort, and endeavor of my parents Dr. Hugo and Mrs. Miriam Gomez. My parents have done everything in their reach to help me become the best I can be, and I hope that I can make them proud and honor them, so that I may see long days on earth. My siblings have also played a vital part in my success; they have been there praying for me, and understanding that my time away is for the better good.

I also want to thank my grandparents for their support through the decades, Mr. Mario Hernandez and Mrs. Maria del Rosario de Hernandez and Mrs. Ruth Estela Vda. de Gomez and Mr. Eliseo Gomez (RIP). I also want to thank each of my siblings Hugo, Gabriel and Christa for being such a great source of support and love.

Nothing of what I am now would be a reality without the work and presence of the man who totally altered my perceptions of life and existence. His influence in me goes far deeper than my mind, it goes past my emotions and instincts, and reaches the innermost cores of my being, Master, my Lord Jesus. Master, I have no words to thank you for what you have done and do for me. I love you Master, and I hope I make you proud. You are my source of strength, my example, my leader, and thank you for telling me that you love me, even though I do not deserve it. I celebrate that you are with me

here, and I believe that I will see you when you come in your glory. To you may be all the glory of whatever I do. Lord, I love you.

My most special and highest gratitude go dedicated to God my Father in Heaven, for shining mercy and grace over me everyday, for giving me His son Jesus, so that I may come home, all majesty and glory and power be given to you now and forever, and when all glory has been given to you, more glory be to you. Father, I love You.

Gratitude and honor go to the Holy Spirit, Parakletos, counselor, guide, and intercessor, thank you for comforting me while my Master comes back. I love You.

# TABLE OF CONTENTS

Page

Page

# LIST OF FIGURES

FIGURE Page

FIGURE Page

FIGURE Page

# NOMENCLATURE

| | |
|---|---|
| MALDI-MS | Matrix Assisted Laser Desorption Ionization Mass Spectrometry |
| AuNPs | Gold Nanoparticles |
| UV-Vis | Ultraviolet-Visible Spectroscopy |
| TEM | Transmission Electron Microscopy |
| NMR | Nuclear Magnetic Resonance Spectroscopy |
| RIY | Relative Ion Yield |
| SAM | Self-Assembled Monolayer |
| BDAC | Benzylcetylammonium Chloride |
| SPR | Surface Plasmon Resonance |

# CHAPTER I

# INTRODUCTION

Mass Spectrometry (MS) is without a doubt one of the most robust techniques for chemical analysis in the advancement of science. It provides rapid, accurate, and precise measurements of molecular masses and a powerful approach for the analysis of complex chemical systems.[1] At the same time, nanomaterials find utility in various applications including enhanced Rayleigh scattering,[2] biological reaction catalysis,[3] aggregation assays,[4] surface enhanced Raman spectroscopy,[5] and other applications known as nanobiotechnology.[6] Therefore, it is the combination of the proven performance of mass spectrometry and the versatility of nanomaterials that drive our desire to study metallic nanoparticles for mass spectrometry based applications.

The initial use of nanomaterials in mass spectrometry traces back to 1988, when Tanaka *et. Al.* applied cobalt nanoparticles (approx. size 30 nm) in glycerol for the analysis of proteins[7] in laser desorption/ionization mass spectrometry (LDI-MS). However, the use of nanomaterials in LDI-MS has historically evolved concurrently with the development and progress of matrix-assisted laser desorption/ionization mass spectrometry (MALDI-MS). In 1988, Karas and Hillenkamp[8] reported the "soft" ionization of biomolecules utilizing organic acid matrices. Since that time, the search for efficient organic acid matrices and their interactions with analyte molecules has been the focus of research aiming at optimizing MALDI experimental conditions.[9-16]

---

This thesis follows the style and format of *Journal of the American Chemical Society.*

On the other hand, in the last two decades, nanomaterial literature contributions demonstrate that nanoscaled materials have promising analytical applications. However, these studies included graphite, silicon, and other materials used for LDI-MS applications with varied results.[17-25] As research progressed, nanomaterials were reported to offer benefits such as extended dynamic range, reproducibility, and sensitivity.[26] The range of applications of nanomaterials for mass spectrometry includes current reports were nanoparticles that have been reported to work as selective and concentrating probes to for matrix assisted laser desorption/ionization-mass spectrometry (MALDI-MS) analysis.[27] Thus, nanomaterials have the potential to allow chemists to obtain materials with unique physical and chemical characteristics that can be exploited for specific applications in mass spectrometry. But not until recently, were gold nanoparticles used for applications in LDI-MS.

Our laboratory has published two reports on the use of gold nanoparticles in mass spectrometry. In the first report, Mclean *et.al.* demonstrated that commercially available gold nanoparticles successfully generated ion signals for peptide analytes.[28] In the second report, Castellana *et. al.* provided experimental evidence demonstrating that capping AuNPs with an efficient proton donor such as 4-aminothiophenol (4-ATP) improved analyte ion yields.[29] In fact, the capped AuNPs increase the protonated analyte $[M+H]^+$ signal over those of the contaminant gold clusters and alkali adducts. In addition, an exhaustive study on the anion effects on the ionization of biological analytes using AuNPs for LDI-MS.[30] However, the scope of nanomaterials does not confine

research to only spherical particles, as we have also studied nanorods for applications in biological mass spectrometry.[31]

In order to better understand the role of the self-assembled monolayer (SAM) on the nanoparticle relative ion yields for LDI-MS applications, we conducted initial experiments altering the molecular structure of the SAMs to alter the photophysical properties of the SAM, and hence, the photophysical properties of the functionalized AuNPs. Considering that AuNPs show an absorption band between 500-600 nm owing to the coherent oscillation of the AuNP conduction band (*i.e.* the surface plasmon resonance), the maximum absorbance ($\lambda_{max}$) of "bare" citrate capped AuNPs is far from the 337 nm and 355 nm laser wavelengths found in conventional laser equipped MALDI-MS instruments as shown in **Fig 1**.

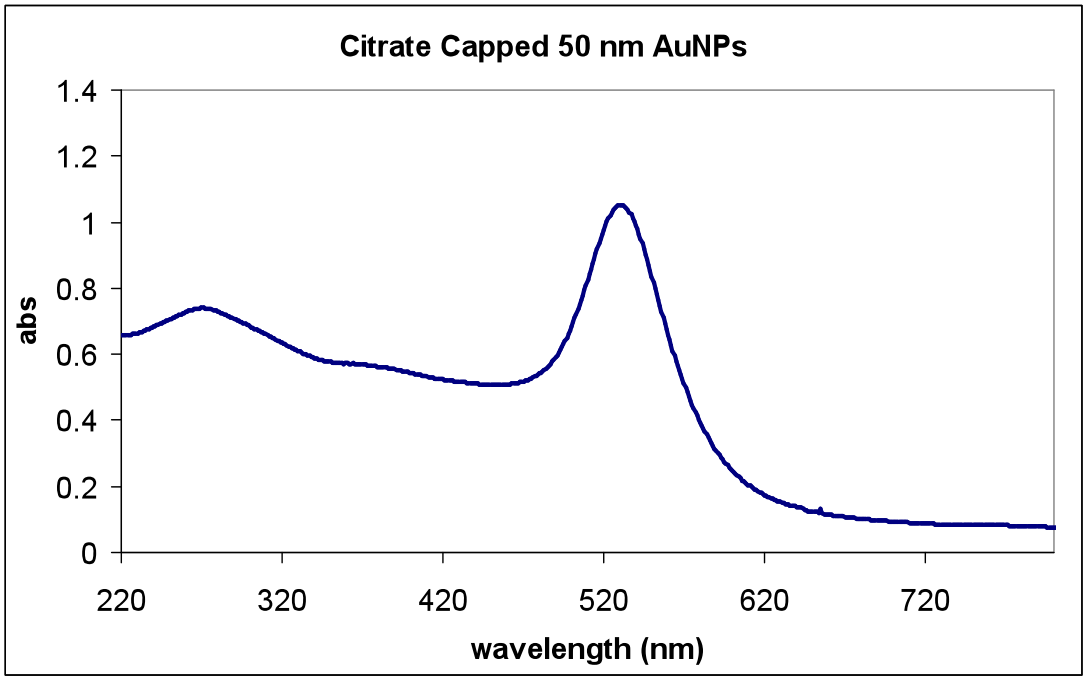


**Figure 1. UV-Vis absorption spectrum of citrate capped 50 nm AuNPs.**

By functionalizing gold nanoparticles with a SAM having strong absorption at around 330-350 nm, the overall absorption of the gold nanoparticle becomes higher at around the 337 nm ($N_2$ Laser) irradiation wavelength, thus making the nanoparticle assembly more efficient for energy transfer to the analyte.

In Chapter II of this document we present data to support our hypothesis that altering the optical properties of the AuNPs by functionalization with a chromophoric SAM improves the relative ion yield of the nanoparticles as a complement to the enhanced ionization obtained with proton donating SAMs. Such postulate becomes feasible as the chromophore serves to "tune" the optical absorption of the AuNPs to values near the 337 nm wavelength. However, it is important to consider that as reported by Castellana *et.al*., the proton donating capabilities of the functional groups found on the monolayer surrounding the nanoparticle have an important role in the increased relative ion yield of the AuNPs. In studying the role of a chromophore bound to the AuNPs, we employed azo type (-N=N-) molecules as SAM on the gold nanoparticles as shown in **Fig. 2**. These experiments provide information on the effect of chromophore suppression on the relative ion yield of the AuNPs by reducing the azo moiety into the hydrazino (-NH-NH-) analogs prior to AuNP functionalization.

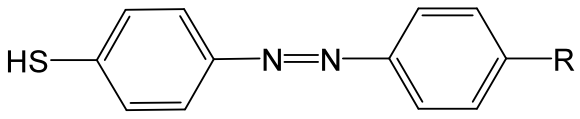


**R= OH, COOH**

**Figure 2. General molecular structure of Azo dye SAM.**

Therefore, our utilized SAMs include phenol and carboxy terminated SAMs of acidic nature on their molecular structure in order to increase protonation of the analytes. In addition, our SAMs have a in the azo chromophore a "tunable molecular switch" that can be used to probe the effect of optical properties of AuNPs in LDI experiments as shown in **Fig. 3**. However, the electron donating/withdrawing characteristics of the functional groups around the SAM also alter the optical properties of the AuNP, i.e. the ($\lambda_{max}$) of the AuNP at 337 nm become higher for AuNPs functionalized with electron donating SAMs, while the electron withdrawing SAMs show little alterations.

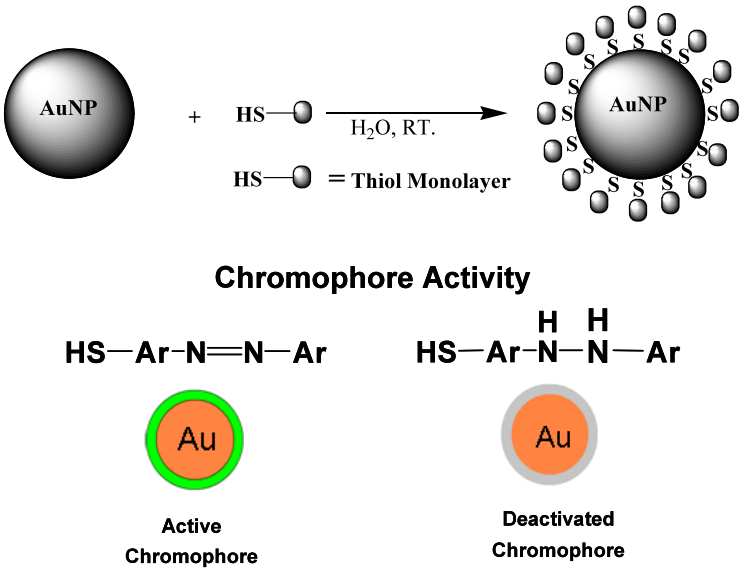


**Figure 3. Cartoon of AuNP functionalization and chromophore deactivation.**

The nature of the functional group either promotes or hinders the free flow of electrons on the AuNPs, depending on the characteristics of the functional group as

depicted in **Fig. 4**. Thus, experiments using a quaternary amine surfactant as preformed ion were designed to rule out the role of proton donation using Benzylcetyldimethilammonium chlrodie (BDAC). By utilizing the preformed ion surfactant as a model analyte, we were able to focus our studies on energy deposition and the relationship between AuNP optical properties and LDI-MS relative ion yields. The preformed ion experiments served to complement the results obtained using the Val$^4$-Angiotensin III peptide (RVYVHPF).

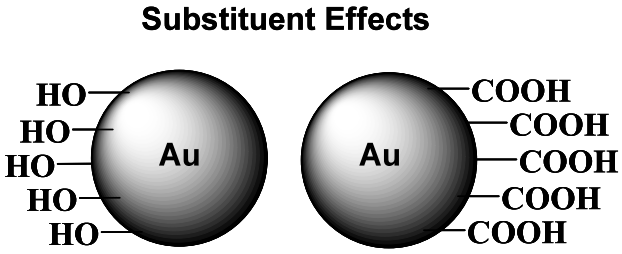


**Figure 4. Cartoon representation of differing SAM substituent group on AuNPs.**

Finally, we discuss the experimental results of our studies regarding the effect of AuNP size on the relative ion yield of the AuNPs under LDI conditions. For the AuNP size studies using 2, 5, 20, 30, and 50 nm AuNPs, we hypothesize that the role of the SAM to enhance energy deposition from the functionalized AuNP unto the analyte decreases as the size of the AuNP increases. That is, with larger AuNP sizes, the energy deposition process from the nanoparticle to the analyte becomes dominated by the photophysical properties of the functionalized metallic core of the AuNP, diminishing the contribution of the nature of the SAM to the energy deposition process. We have also studied the identity of the major peak signals observed in our mass spectra for the AuNP

size studies. By closely monitoring the ratio of the abundances of the atomic gold ion $Au^+$ and subsequent clusters (i.e., $Au_2^+$, $Au_3^+$, etc) in relation to the analyte ion, we have observed interesting relationships between the different types of ions as a function of AuNP size. Such relationships then can be used to support our hypothesis that as the size of the AuNP increases, the energy deposition processes on the functionalized AuNPs also change, due to the differences in energy dissipation experienced by the AuNPs of different sizes. As shown in Chapter III, our tabulated results show that 5 nm AuNPs had the lowest abundances of gold clusters in relation to the abundance of the analyte ion. Such correlation supports the fact that as the absorption of the active monolayer is higher at 5 nm, the impact of the SAM on the relative ion yields is more evident on the 5 nm AuNPs in LDI experiments.

# CHAPTER II

# EFFECTS OF CHROMOPHORE DEACTIVATION ON THE RELATIVE ION YIELDS OF FUNCTIONALIZED GOLD NANOPARTICLES FOR LDI-MS APPLICATIONS

## Introduction

Considering that the chemical and optical properties of the AuNPs depend on both, the composition of the core and the molecular structure of the SAMs[32-33], with each of these two components having different contributions to the properties of the AuNP. The chromophore deactivation studies are intended to investigate the mechanism of analyte LDI from monolayer capped AuNPs. In particular, we wanted to understand the effects that subtle changes to the monolayer structure have on analyte ionization efficiencies when using azo (-N=N-) capped AuNP in LDI-MS. For our experiments, a series of our two novel azo dyes and their reduced Hydrazine analogs were prepared and used as self-assembled monolayers (SAMs) on AuNPs. However, for comparative purposes, two non-chromophore mono-substituted aromatic thiols were also employed as SAMs. These two non-chromophore aromatic thiols had the same terminal groups as our azo dyes (i.e. OH and COOH) to compare the RIY of both assemblies against the azo functionalized AuNPs to study the influence of the chromophore in the LDI process. As shown in **Figure 5,** the structures of the monolayer molecules used in this study gradually vary among themselves from non-chromophore, to deactivated chromophore, to active chromophore. Furthermore, in order to study the role of the monolayer in analyte

ionization, our experiments aimed to compare the analyte ion yields of two types of analytes. First, we studied RIYs using the peptide Val$^4$-Angiotensin III (RVYVHPF) to monitor the AuNPs with molecule of biological relevance. Secondly, we studied the RIYs using the Benzylcetyldimethylammonium chloride (BDAC) surfactant, to study RIYs using a pre-formed ion approach. Both sets of experiments were designed to analyze the consistency of the RIY correlations in spite of the analyte. However, for both sets of experiments (peptide and surfactant analytes) our results showed that the RIY of the AuNPs is significantly dependent on the molecular characteristics of the monolayer with the ionization trends remaining constant in spite of the identity of the analyte.

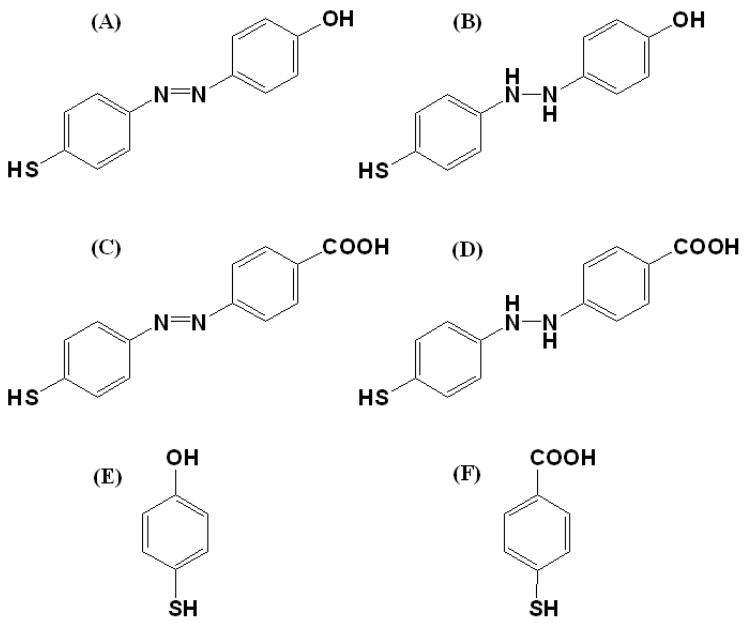


**Figure 5. Structures, names and abbreviations of utilized SAMs:**
**(A) 4-(4-Mercapto-phenylazo)-phenol (AzP),**
**(B) 4-[N'-(4-Mercapto-phenyl)-hydrazino-phenol (Hy-AZP),**
**(C) 4-(4-Mercapto-phenylazo)-benzoic acid (Az-4BA),**
**(D) 4-[N'-4-Mercapto-phenyl)hydrazino-benzoic acid (Hy-Az-4BA),**
**(E) 4-Mercaptophenol (MP)**,
**(F) 4-Mercaptobenzoic Acid (MBA).**

As the metal nanoparticle and the monolayer have both distinct contributions to the optical properties of the assembly, it is important to study which component carries the bulk of the absorption and transfer of energy for the ionization/desorption of the analyte. Therefore, in order to better understand and distinguish the role of the chromophore on the monolayer, against that of the gold nanoparticle, a chemically "switchable" molecular functionality was used. By "turning off" the active chromophore on the monolayer, changes in the relative ion yield of the capped nanoparticles can be evaluated and correlated to the changes in absorption of the monolayer/gold nanoparticle assembly. For the present work, inspired by the azo (-N=N-) chromophore found in the well documented (2-(4-Hydroxyphenylazo)-benzoic acid **(HABA)**[34] molecule shown in **Fig. 6**, "turning off" the chromophore in the SAM should directly affect the relative ion yield of the functionalized AuNPs while keeping the metallic core of the nanoparticle unaltered.

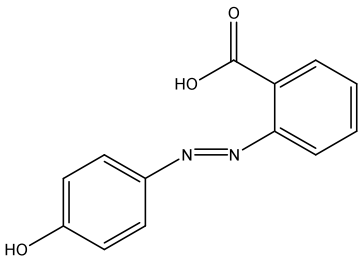


**Figure 6. Molecular structure of 2-(4-Hydroxyphenylazo)-benzoic acid (HABA).**

Considering that azo dyes have optical absorption bands near the 337 nm and 355 nm wavelengths,[35,36] this class of molecules is highly appropriate for experiments using a conventional MALDI mass spectrometer (DE-STR MALDI-TOF Mass Spectrometer, Applied Biosystems, Foster City, CA). Our experiments consisted of the preparation of

two novel thiol azo SAMs and their respective reduced Hydrazino analogs. Each molecule was then utilized as a SAM on gold nanoparticles as shown in **Fig. 7**.

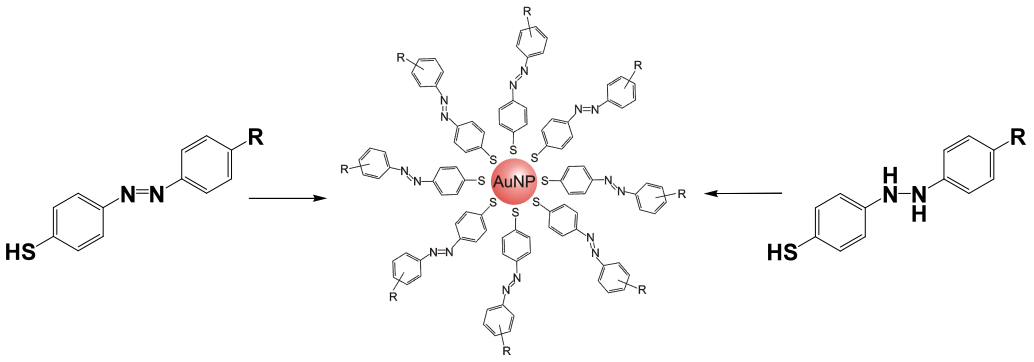


**Figure 7. Azo dye and hydrazino monolayer general template. R= OH, COOH.**

## Experimental

*Monolayer Synthesis and Characterization*

The azo compounds were prepared in our laboratory using a diazonium salt synthetic route, with subsequent workup for cleaning purposes.[37] Both azo compounds were assigned a name and abbreviation as shown below were (Az) denotes the common (4-mercapto-phenylazo) structure as shown in **Fig. 8.** Characterization of the obtained monolayers was obtained through 300 MHz. Nuclear Magnetic Resonance (VARIAN 300 MHz NMR) and Electrospray Ionization Mass Spectrometry (QSTAR-ESI-MS).

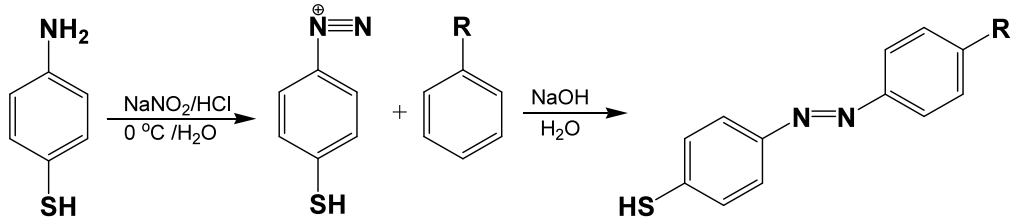


**Figure 8. Diazonium salt synthetic route used in the preparation of substituted azo monolayers from substituted aromatic precursors. Az= (4-mercapto-phenylazo), R= (COOH, OH).**

*Preparation of Hydrazino Analogs*

Azo dyes were reduced into the hydrazino analogs by reduction of the azo choromophore (-N=N-) with Hydrazine Monohydrate in Ethanol.[38] The process generated the deactivated non chromophore hydrazino (-HN-NH-) functionality as shown in **Fig. 9.**

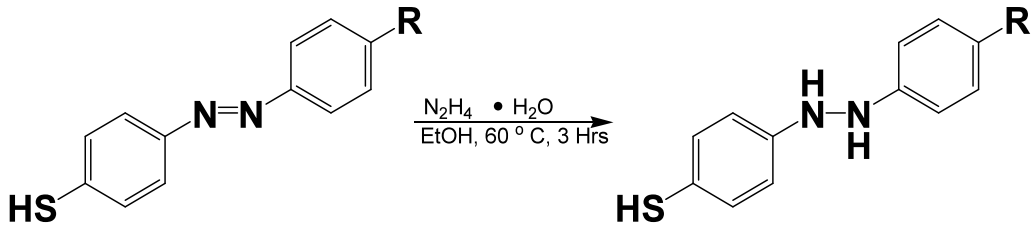


**Figure 9. Preparation of hydrazino analogs. Reduction of the azo functionality was conducted with hydrazine monohydrate in Ethanol.**

*Synthesis and Characterization of Functionalized Gold Nanoparticles*

For the preparation of the functionalized gold nanoparticles, commercially available citrate capped AuNPs (Ted Pella Inc. Redding, CA.) were incubated with each set of active azo and hydrazino SAMs. In this approach, the free thiol azo monolayer was added in 10-fold excess to ensure complete coverage of the surface of the nanoparticle. The AuNPs were obtained with an approximate particle size of 5 nm as determined by JEOL Transmission Electron Microscopy (TEM) as shown in **Fig. 10**. Imaging data was obtained on a JEOL 2010 TEM instrument, with a 200kV accelerating voltage using a dried .5- 1 μL drop dried droplet method on a cupper grid (Ted Pella Inc. Redding, CA)

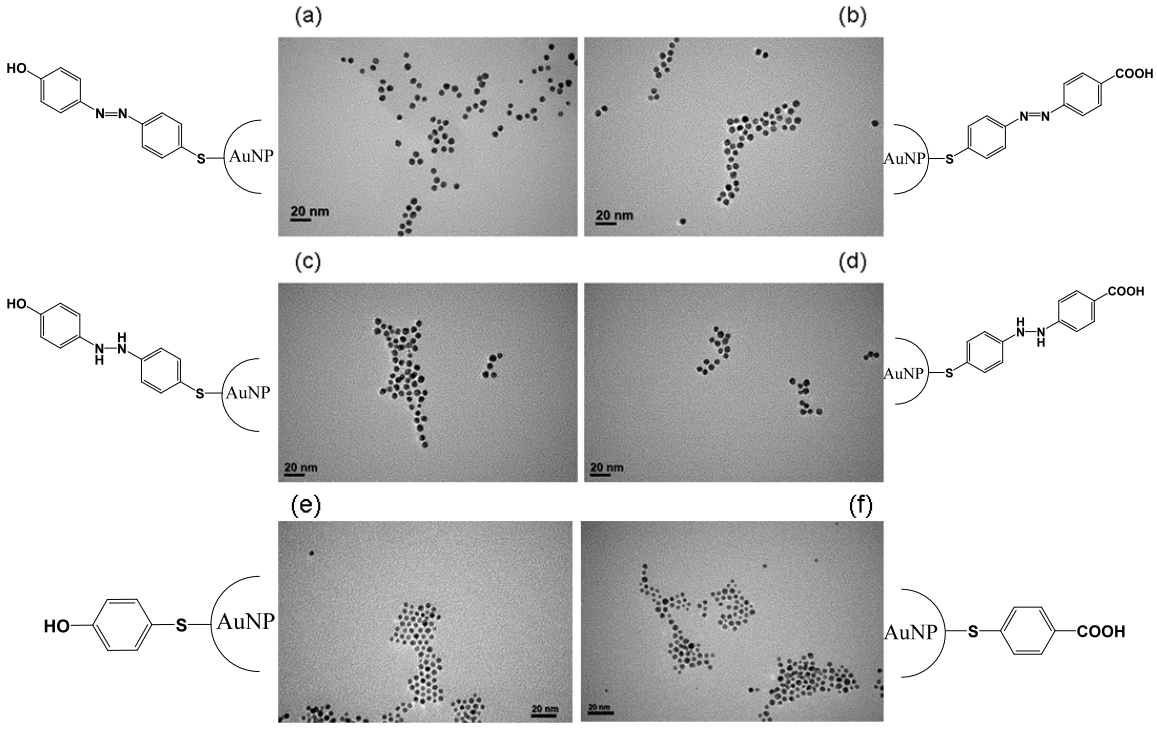


**Figure 10. Azo and hydrazino monolayer functionalized nanoparticles: (a) AzP@AuNP, (b)Az-4BA@AuNP, (c) Hy-AZP, (d) Hy-Az-4Ba, (e) MP@AuNP, and (f) MBA@AuNP. Approx. size: 5 nm. Scale Bar= 20nm, Mag. 80K Micrographs were obtained at the Microscopy and Imaging Center at Texas A&M University with a JEOL 2010 instrument.**

*337 nm Nitrogen Laser Calibration*

Laser energy measurements were taken using an Ophir Nova Power/Energy meter coupled to a PE-10 Ophir Pyroelectric head (Ophir Laser Measurement Group,North Logan, UT). Measurements were taken in increments of 50 arbitrary units on the rotatable variable neutral density filter wheel used on the MALDI-TOF Voyager DE-STR (Applied Biosystems, Foster City, CA).

Values were recorded every 200 shots from a total of 1400 laser shots per setting point in the lower energy region (0.77 - 1.92 μJ) of the laser, and every 100 arbitrary

units on the higher energy region of the laser (1.92 - 51.89 μJ). The process was repeated twice and the average calculated.

*Laser Desorption Ionization Mass Spectrometry*

All mass spectrometry experiments were conducted on the Applied Biosystems DE-STR MALDI-TOF (Foster City, CA) instrument using a $N_2$ 337 nm Laser set up (Spectra-Physics, Irvine, CA). The applied accelerating voltage was set at 25 kV, the grid percentage was set at 65%, and delayed extraction time of 200 ns. The MS data was acquired using the positive ion mode using the reflectron mode analyzer on the mass spectrometer.

Typically, 15 μL of the AuNPs solution were mixed with 15 μL of the 1 mg/mL $Val^4$-Angiotensin III (RVYVHPF) or 0.001 mM BDAC solution, and a 1 μL aliquot was deposited on the stainless steel MALDI-MS plate. An array of dried droplet spots were deposited on the MALDI plate and each spot interrogated once with 200 shots/spectrum. The average of 4 spectra was used to calculate the data points plotted in all relative ion yield comparison plots.

**Results and Discussion**

The AuNPs functionalized with a conjugated azo chromophore (-N=N-) provide greater analyte ion yields compared to the AuNPs capped with the hydrazino analogs or the mono-substituted aromatic thiols. **Figure 11** contains plots of $[M+H]^+$ ion yield vs. applied laser energy (μJ/shot) for the analyte $Val^4$ Angiotensin III (RVYVHPF) obtained from 5nm AuNPs capped with the compounds listed above (see **Figure 6**).

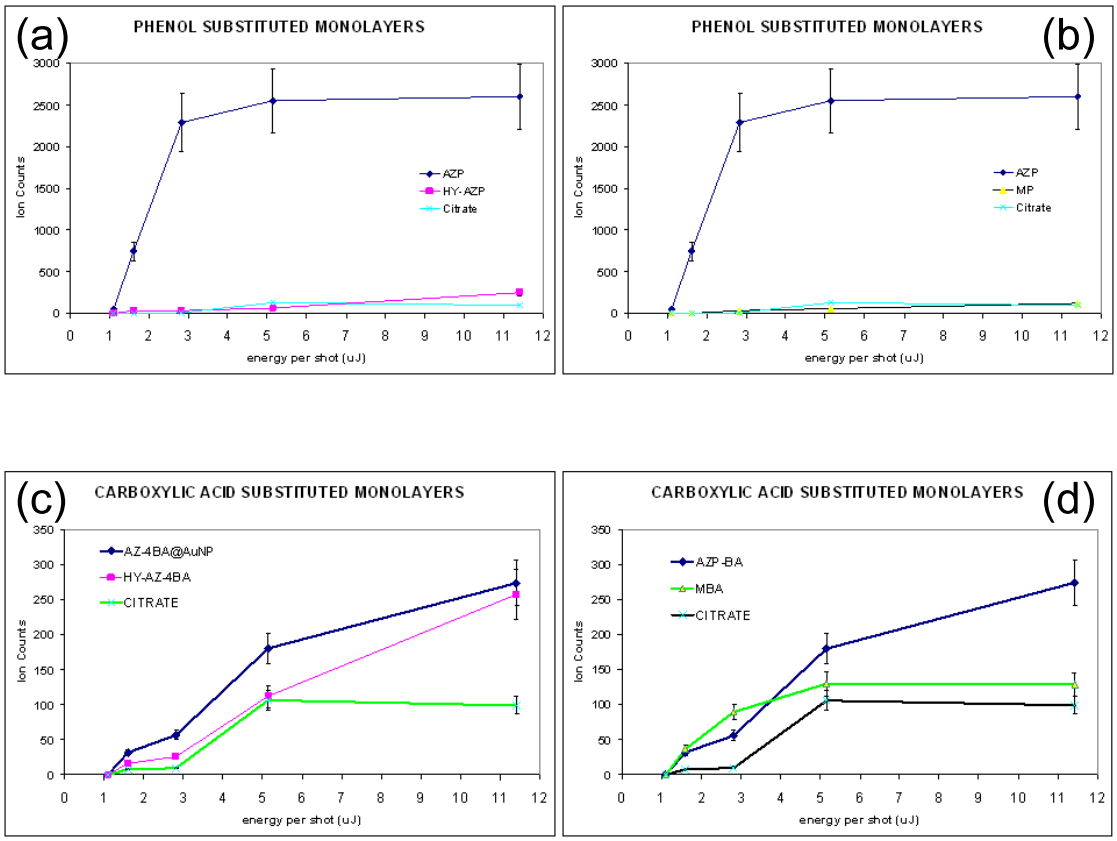


**Figure 11. Panel (a): Relative ion yield comparison for active chromophore (AZP) functionalized AuNPs vs suppressed chromophore (Hy-AZP) functionalized AuNPs. Panel (b): relative ion yield comparison for active (AZP) chromophore functionalized AuNPs vs. 4-mercaptophenol (MP) functionalized AUNPs. Panel (c): relative ion yield comparison for active chromophore (Az-4BA) functionalized AuNPs vs suppresed (Hy-Az4Ba) chromophore functionalized AuNPs. Panel (d) relative ion yield comparison for active (Az-4BA) functionalized AuNPs vs. 4-mercaptobenzoic acid (MBA) functionalized AUNPs. Val4 Angiotensin III was used as analyte in both data series.**

The increased ion yields for the phenol substituted azo chromophore capped AuNPs vs. the reduced hydrazine analog may be the result of loss of conjugation of this extended pi system; however, these capped AuNPs also show enhanced absorbance at 337nm as depicted in **Fig. 12**, left panel, series (A). Thus, the relatively higher ion yields for the azo chromophore capped AuNPs can be correlated to the relative differences in the UV-vis spectra of the capped AuNPs. For example, we have observed lower ion

yields from carboxylic acid containing azo compounds (AZ-4BA@AuNPs) than for the phenol terminated analog (AZP@AuNP). Also, within the carboxyl family, the azo chromophore produces more ions than the reduced analog and the hydrazino substituted aromatic thiol.

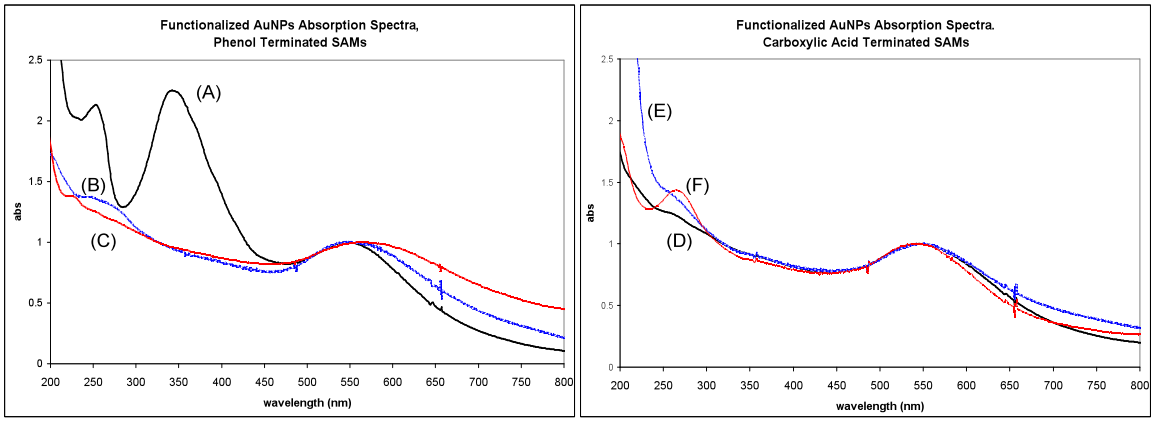


**Figure 12. UV-vis absorption spectra for functionalized AuNPs. The left panel contains data for the following phenol terminated SAMs on AuNPs: (A) AZP@AuNPs, (B) Hy-AZP@AuNPs, (C) 4-MP@AuNPs. The right panel contains data for the following carboxylic acid terminated SAMs on AuNPs: (D) AZ-4BA@AuNPs, (E) Hy-AZ-4-BA@AuNPs, (F) 4-MBA@AuNPs.**

Note that the AZP capped AuNPs generate higher analyte ion yields than did the all other monolayer capped AuNPs. Again, the AZP capped AuNPs, with the highest absorption of the laser, produce enhanced ion yields for the analyte. In the data for $Val^4$-Angiotensin III and BDAC, the general trend correlating analyte ion yield and optical absorption is preserved. That is, an increase in UV absorption correlates with an increase in analyte ionization. The results support the hypothesis that AuNPs with higher optical absorption and modified with a conjugated chromophore have higher efficiency for laser energy transfer to promote analyte desorption and ionization. The chromophore suppression studies were aimed to demonstrate that the relative ion yield

of the AuNPs capped with the active azo (-N=N-) chromophore SAM is higher than the relative ion yield of the suppressed chromophore (–HN-NH-) functionalized AuNPs. It also demonstrates that AuNPs having an active chromophore had higher relative ion yields than AuNPs functionalized with aromatic thiols such as 4-Mercaptophenol 4-MP and 4 Mercaptobenzoic 4-MBA acid. These results demonstrate the relationship between the differences in UV-Vis spectra between the active (azo) and suppressed (hydrazino) monolayers mounted on the AuNPs and the 4-MP and 4-MBA functionalized gold nanoparticles. The LDI-MS data demonstrates that the relative ion yield of the AuNPs functionalized with an active azo chromophore SAM is higher than that of the nanoparticles capped with a suppressed chromophore. Therefore, the data in **Fig. 11** provides a correlation of the protonated analyte $[M+H]^+$ ion counts vs. the applied laser energy showing the differences in results from both series of nanoparticle assemblies.

Overall, the data showed that the relative ion yield of the hydrazino SAMs decreased with respect to the azo capped AuNPs. The higher ion yields of the AuNPs capped with the active chromophores can be correlated to the differences in the UV-Vis absorption spectra of each set of AuNPs. That is, AuNPs capped with the active chromophore SAM termed AZP, have higher UV-Vis absorption near the 337 nm wavelength, which in turn promote higher ion yields for the analyte than those AuNPs functionalized with a non chromophore SAM. The correlation of these results provides experimental evidence supporting the original hypothesis that an active chromophore on the AuNP increases the relative ion yield of the assembly. However, as the vast improvement observed with the phenol substituted azo dye over the hydrazino analog

might be attributed to the strong absorbance near the 337 nm wavelength. The nanoparticles functionalized with the carboxylic acid functionalized azo SAM, while still producing higher ion yields than the respective hydrazino analog assemblies, had quite lower performance than the phenol substituted azo SAM.

In order to explain the different performance of the functionalized AuNPs, the characteristics of the functional group on the SAMs must be considered. Thus, the vast changes observed in the absorption spectra of the functionalized AuNPs (shown in **Fig. 12)** might be attributed to a combination effect of the optical characteristics of the SAMs and the nature of the substituent groups found on each class of capping molecules.

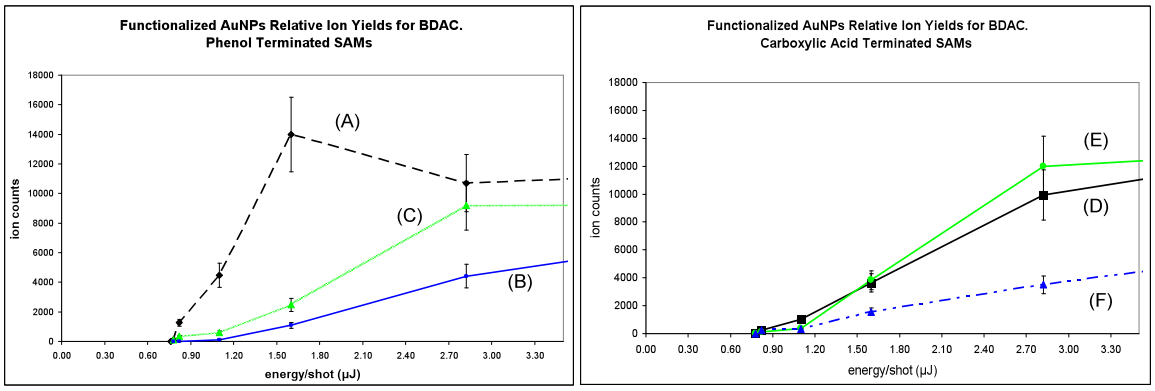


**Figure 13. Comparison of relative LDI (337 nm) ion yields for functionalized AuNPs for BDAC at 337 nm. The left panel illustrates ion yields for phenol terminated SAMs: (A) AZP@AuNPs, (B) Hy-AZP@AuNPs, (C) 4-MP@AuNPs. The right panel illustrates ion yields for carboxylic acid terminated SAMs: (D) AZ-4BA@AuNPs, (E) Hy-AZ-4BA@AuNPs, (F) 4-MBA@AuNPs.**

To further analyze the role of the chromophore in the desorption/ionization process, we have tested the AuNPs with the analyte Benzylcetyldimethylammonium Chloride (BDAC). In such experiments, considering that the analyte is a quaternary amine surfanctant, thus having a charge on the central nitrogen, it does not need to gain a

proton to obtain a charge. Hence, the role of the functional group is ruled out, and only the optical absorption of the chromophoric nanoparticle assembly drives the desorption of the analyte. **Fig. 13** shows data where the patterns of nanoparticle relative ion yield remain, (*i.e.* the active AZP monolayer being more efficient than the reduced analog SAM), even when utilizing the preformed ion analyte BDAC.

From the data, it is viable to say that the increased absorbance of the nanoparticles around 337 nm does increase the ion survival and desorption of the analyte as shown in **Fig. 13**. From the pre-formed ion experiments it is also evident that the RIYs of the AuNPs functionalized with the active chromophore SAMS generated higher RIYs than the AuNPs functionalized with the aromatic non-chromophore thiols. **Fig. 13** also shows that even when the RIY using the azo chromophore monolayer is higher for the OH terminated SAM, the RIY of the AuNPs functionalized with the COOH terminated SAM becomes very similar to the RIY of the deactivated SAM. This trend can be correlated to the similar optical absorption of the AuNPs capped with COOH group, where both the active and suppressed chromophores have similar UV-Vis absorption at around 320-340 nm as shown above in **Fig. 12**. Since the absorption of such AuNPs is similar, then, it is not surprising to see that the patterns in RIY of these AuNPs are similar as well.

**Summary**

The results provide experimental evidence that the presence and activity of a chromophore on the molecular frame of the SAM is beneficial for the desorption/ionization process of the AuNPs in LDI-MS. Results also suggest that the identity of the proton donating functional groups has a role in analyte ionization as demonstrated in the ionization trends using the two different functional groups on the SAMs. But the identity of the functional group is also dependant on the electron donating and withdrawing character of the functional group. As the data clearly showed, phenol substituted SAM have higher ion yields than the carboxylic acid terminated SAMs. Therefore, the capacity of the SAM to conduct energy deposition to the analyte is not solely governed by the gas phase proton affinity of the SAM, but by the capacity of the SAM to conduct and delocalize energy through its molecular frame to the analyte.

As demonstrated by the pre-formed ion experiments, the phenol substituted azo SAM still had higher ion yields than the carboxy substituted azo SAM, even when protonation was not part of the LDI process using the BDAC molecule as model analyte. As the data suggests, the enhanced optical absorption of the phenol terminated azo SAM correlates to enhanced energy deposition by the nanoparticle to the analyte. The observed correlation remains regardless of the need for proton transfer. Therefore, it can be posited that the electron donating or withdrawing character of the SAM also affects the capacity of the functionalized AuNP to conduct energy deposition to the analyte and promote ion formation in LDI experiments. Thus, the electron donating character of the phenol group seems to aid in the energy deposition process, as it also promotes enhanced

optical absorption by the SAM. In the other hand, the electron withdrawing character of the carboxylic acid group did not show enhanced optical absorption, and thus, the RIY using the carboxy terminated SAM were lower. The data suggests that if the optical absorption of the AuNPs remains similar for the functionalized AuNPs of the same terminal group type, then the RIY patterns will be similar between AuNPs sets regardless of the identity of the analyte. On the other hand, if the optical absorption of the AuNPs shows large differences, as is the case in the OH terminated azo SAM group, the RIY patterns shown marked differences between AuNP sets, regardless of the identity of the analyte. Our data then suggest that there is a close relationship between AuNP absorption, and AuNP RIY.

# CHAPTER III

# VARIATIONS OF GOLD NANOPARTICLE LASER DESORPTION IONIZATION RELATIVE ION YIELDS AS CONSEQUENCE OF SIZE

## Introduction

In the literature, previous studies have shown that as the nanoparticle diameter increases, the surface area of each nanoparticle also increases, causing the SPR absorption band to red shift and increases in intensity.[39] In addition, as the size of the nanoparticle increases, the surface area of the AuNP becomes larger causing for changes in the thermal properties of the AuNPs.[40] These changes in the physical and chemical properties of the particles alter the optical properties of the AuNPs[41,42], and thus may also alter capacity of the AuNP to dissipate energy after excitation. Additionally, changes in NP size alter the capacity of the AuNPs to dissipate energy to their surroundings during/following laser irradiation. We have investigated the effect of AuNP size on the resulting analyte ion yields for LDI-MS. For these studies, we have compare the relative ion yield of azo SAM functionalized AuNPs of sizes 2, 5, 20, 30, and 50 nm using Laser irradiation at 337 nm.

Another important factor affecting the photophysical properties of AuNPs is the fact that as the size of the AuNP increases, the length of the SAM remains constant at about 12 Å as depicted in **Fig. 14**. Therefore, with increasing AuNP diameter, the relative thickness of the SAM layer with respect to the overall circumference of the AuNP decreases dramatically. Thus, we postulate that the change in relative thickness of the SAM around the monolayer directly affects the photophysical properties of the

AuNPs as recorded in the changes in the UV-Vis spectra of the functionalized AuNPs. Such changes in the optical properties of the AuNPs alter the energy deposition properties of the AuNPs, directly affecting the relative ion yield of the AuNPs during LDI experiments with the Val$^4$-Angiotensin III (RVYVHPF) peptide or the BDAC surfactant.

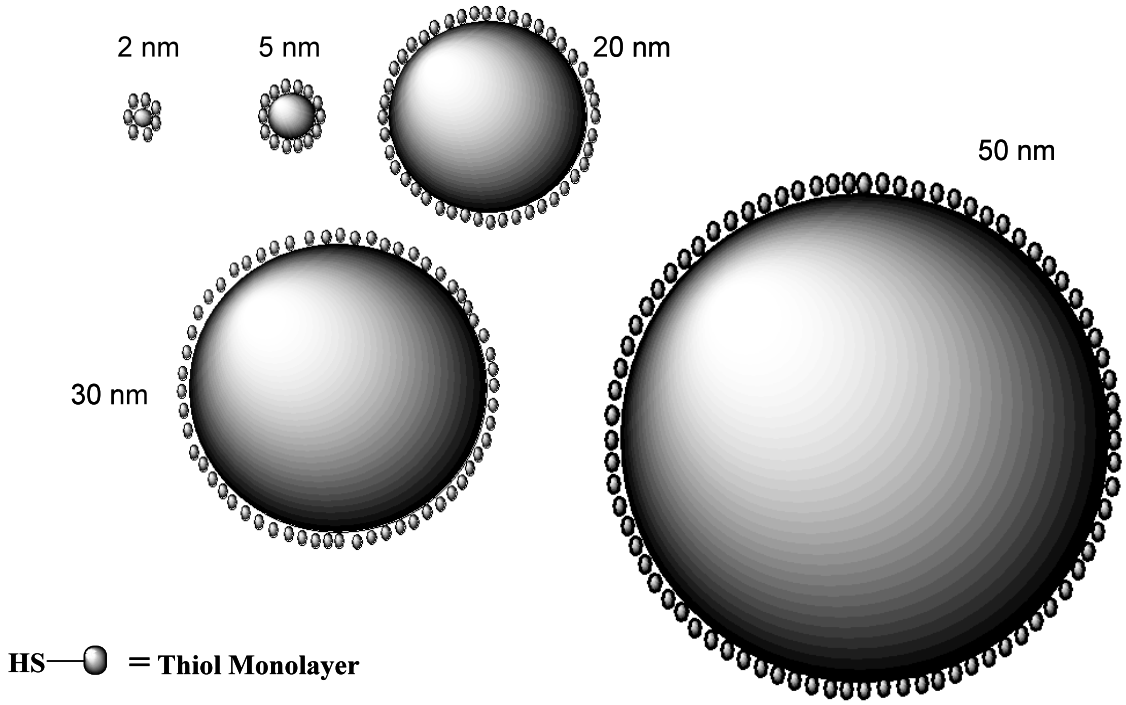


**Figure 14. Representation of the dramatic increase in AuNP sizes drawn to scale.**

## Experimental

All reactions were carried out under an argon atmosphere in oven-dried glassware with magnetic stirring. All commercially obtained reagents were used as received. Water was distilled and deoxygenated under nitrogen flush.

Cooling was accomplished using an ice bath. Purification of reaction products was carried out by flash column chromatography using silica gel or by recrystallization. TLC visualization was accompanied with UV light. $^{1}$H NMR spectra were recorded at 300 MHz, and are reported relative to acetone-d6 (δ 2.05). $^{1}$H NMR coupling constants (J) are reported in Hertz (Hz) and multiplicities are indicated as follows: s (singlet), d (doublet), t (triplet), m (multiplet). Proton-decoupled $^{13}$C NMR spectra were recorded at 75 MHz and reported relative to acetone-d6 (δ 29.92).

*Procedures and Characterization Data*

Compound **1** and **2** are new compounds. Full-tabulated data is available below for both of them.

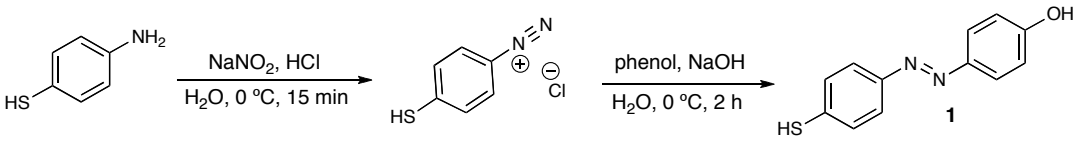


**Figure 15. Scheme of reaction for AZP dye synthesis.**

**(*E*)-4-((4-mercaptophenyl)diazenyl)phenol** (**1**)**:** *p*-aminothiophenol (250 mg, 2 mmol) was dissolved in a solution of $H_2O$ (10 ml) and conc. HCl (1.0 ml). The solution was cooled to 0 ºC on an ice-water bath. A cold solution (0 ºC) of aqueous $NaNO_2$ (145 mg,

2.1 mmol in 10 ml) was added over a period of 3 min. Reaction conditions are summarized in **Fig. 15**.

The solution of diazonium salt was added dropwise to a cold (0 ºC) and stirred solution of phenol (225 mg, 2.4 mmol) NaOH (400 mg, 10 mmol) in $H_2O$ (10 ml). The mixture immediately became colored (dark orange).

After 2.5 h at 0 ºC the brownish orange mixture was neutralized by addition of dilute aqueous hydrochloric acid. A brownish orange precipitate was formed and filtered off. This crude product was purified by chromatography on a silica column (Hexanes/EtOAc 1:1) to yield 308 mg (67%) of **1** as yellow-orange crystals.

Characterization data obtained for IR (ATR) $\nu$ $^{3586, 3230, 2014, 1738, 1588}$, 1382, 1250, 838 $^{cm1;}$ Nuclear Magnetic Resonance data was obtained for the compound with the following signal peaks: $^{1}$H NMR (acetone-d6) δ 9.23 (bs, 1OH), 7.89–7.83 (m, 4H), 7.44 (d, $J$ = 8.8 Hz, 2H), 7.01 (d, $J$ = 7.2 Hz, 2H), 2.98 (s, 1SH); as shown in **Fig. 16**. $^{13}$CNMR (acetone-d6) $\delta$ 161.8, 152.9, 147.1, 139.5, 128.8, 125.9, 124.1, 116.8; as shown in **Fig. 17**. UV–Vis $\lambda$max ($\varepsilon$) 370 nm; (ESI) calculated for $C_{12}H_{10}N_2OS$ requires *m/z* 230.0513, found 230.0331.

## $^{1}H$ and $^{13}C$ NMR Spectra

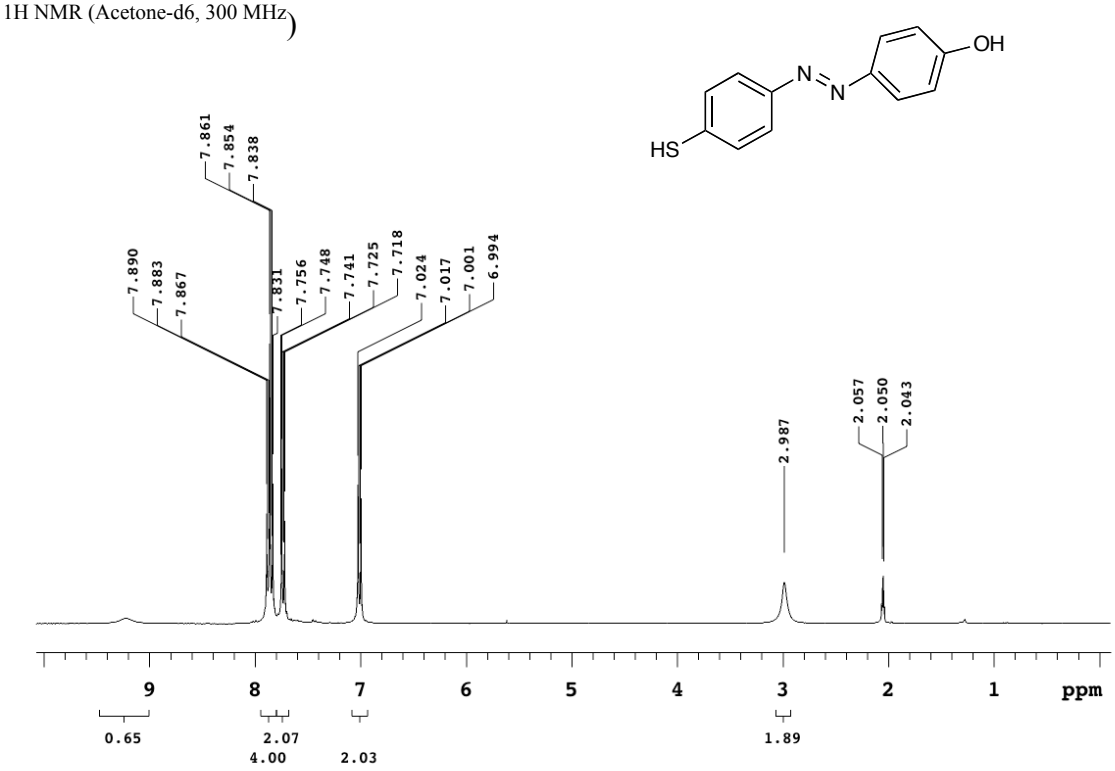


**Figure 16. Proton NMR spectrum of AZP.**

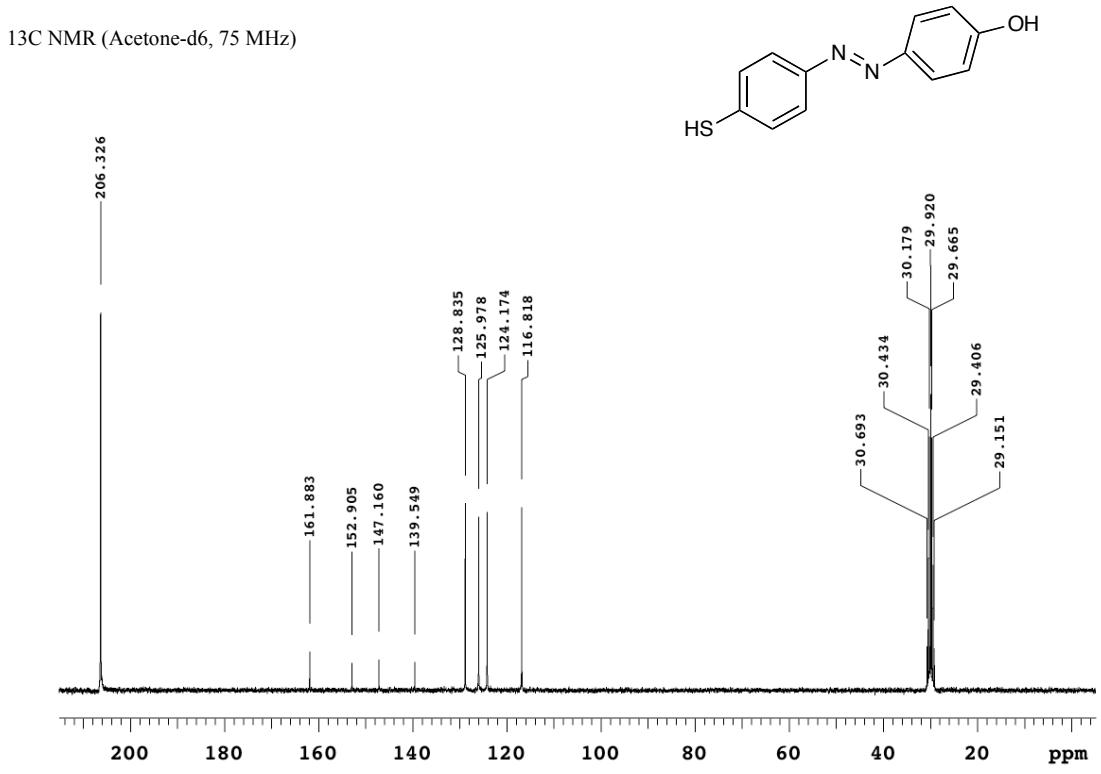


**Figure 17. Carbon NMR spectrum of AZP.**

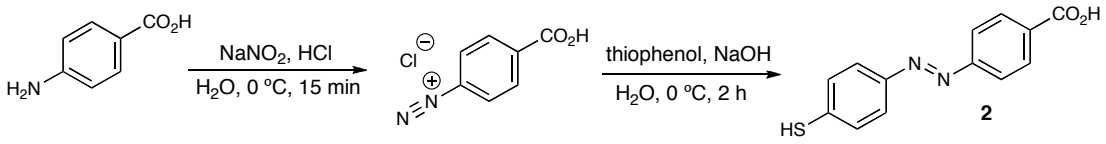


**Figure 18. Scheme of reaction for AZ-4BA synthesis.**

**(*E*)-4-((4-mercaptophenyl)diazenyl)benzoic acid (2):** *p*-aminobenzoic acid (275 mg, 2 mmol) was dissolved in a solution of $H_2O$ (10 ml) and conc. HCl (1.0 ml). The solution was cooled to 0 ºC on an ice-water bath. A cold solution (0 ºC) of aqueous $NaNO_2$ (145 mg, 2.1 mmol in 10 ml) was added over a period of 3 min. Reaction conditions are summarized in **Fig. 18**. Utilizing clean glassware, the solution of diazonium salt was added dropwise to a cold (0 ºC) and stirred solution of thiophenol (260 mg, 2.4 mmol) and NaOH (400 mg, 10 mmol) in distilled $H_2O$ (10 ml). The mixture became colored (yellow) immediately. After 2.5 h at 0 ºC, the yellow mixture was neutralized by addition of dilute aqueous hydrochloric acid.

A bright yellow precipitate was formed and filtered off. This crude product was purified by recrystallization from acetone to yield 403.5 mg (78%) of **2** as yellow-orange crystals. Characterization data obtained for IR (ATR) $\nu$ $^{3729, 3062, 2047, 1678, 1577}$, 1378, 1288, 850 $^{cm1}$. Nuclear Magnetic Resonance data was obtained for the compound with the following signal peaks: $^1$H NMR (acetone-d6) δ 8.15 (d, $J$ = 6.9 Hz, 2H), 7.76 (d, $J$ = 6.6 Hz, 2H), 7.66 (d, $J$ = 6.6 Hz, 2H), 7.55 (d, $J$ = 9.3 Hz, 2H); as shown in **Fig. 19**. $^{13}$CNMR (acetone-d6) $\delta$ 166.9, 155.1, 134.3, 132.6, 131.9, 131.8, 130.6, 130.4, 122.3; as shown in **Fig. 20**. UV–Vis $\lambda$max ($\varepsilon$) 340 nm; (ESI) calculated for the formula $C_{13}H_{10}N_2O_2S$ [M–H] requires *m/z* 257.0385, found 257.0225. The obtained analytical

data allowed for the confident determination of the molecular structure of the synthesized azo dyes with high purity. The isolated compounds were stored in a dry environment chamber for preservation and further application in the functionalization of the AuNPs.

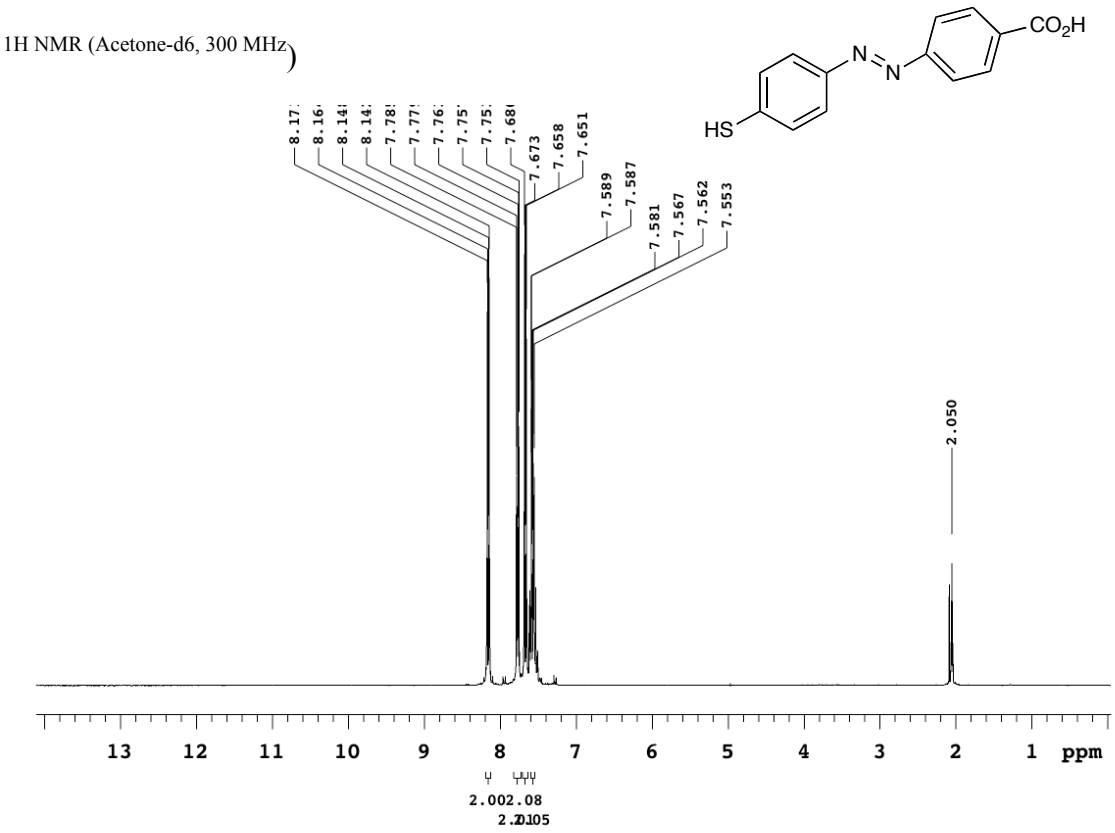


**Figure 19. Proton NMR spectrum of AZ-4BA.**

13C NMR (Acetone-d6, 75 MHz)

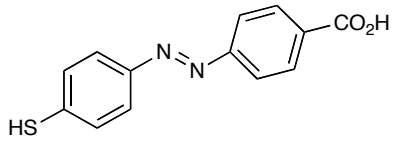


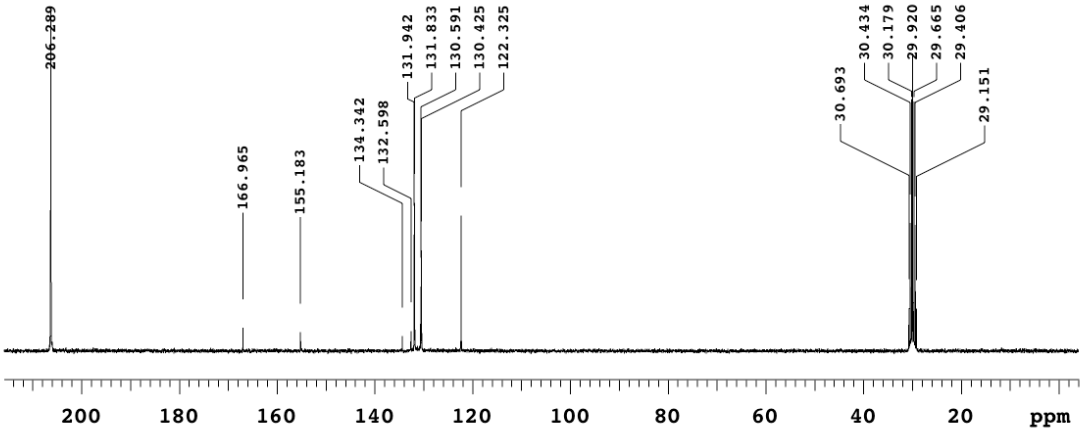


**Figure 20. Carbon NMR spectrum of AZ-4BA.**

*Gold Nanoparticle Functionalization*

2 nm Gold Nanoparticle Functionalization and Clean Up

Typically, a 100 µL aliquot of the 2 nm AuNP was mixed with 10 uL of either of the azo dye stock solutions (2 mg/mL). Such excess was necessary to ensure that the AuNPs were completely coated under the monolayer exchange mechanism. The nanoparticles were allowed to incubate overnight (a minimum of 12 hours). Thereafter, the 2 nm AuNPs were further incubated with 800 µL of 50 nm AuNP to remove excess dye from the previous incubation. The secondary incubation was allowed to continue overnight. The AuNPs were then separated by centrifugation to separate the 50 nm scavenging AuNPs. It is important to note that as the 2 nm AuNPs are small, they do not coagulate in the bottom of the sample tube. Therefore, separation from the 50 nm AuNPs is very efficient.

5 nm Gold Nanoparticle Functionalization

Typically, a 100 uL volume of the 5 nm AuNP was mixed with 10 µL of either of the azo dye stock solutions ( 2 mg/mL). As with the 2 nm AuNPs, such excess was necessary to ensure that the AuNPs were completely coated under the monolayer exchange mechanism. The nanoparticles were allowed to incubate overnight (a minimum of 12 hours). After the incubation period was complete, the AuNPs were cleaned by centrifugation at 14000 rpms and resuspended in clean ultra pure water followed by sonication for 20 minutes. The clean up steps were required to remove excess azo dye SAM from the AuNP preparation mixture.

20 nm Gold Nanoparticle Functionalization

Typically, a 100 µL volume of the 20 nm AuNP was mixed with 1 µL of either of the azo dye stock solutions ( 2 mg/mL). As with the 2 nm AuNPs, such excess was necessary to ensure that the AuNPs were completely coated under the monolayer exchange mechanism. The nanoparticles were allowed to incubate overnight (a minimum of 12 hours). After the incubation period was complete, the AuNPs were cleaned by centrifugation at 4000 rpms and resuspension followed by sonication for 20 minutes The clean up steps were intended to remove excess azo dye SAM from the AuNP preparation mixture.

30 nm Gold Nanoparticle Functionalization

Typically, a 100 µL volume of the 30 nm AuNP was mixed with 1 uL of either of the azo dye stock solutions ( 2 mg/mL). As with the 2 nm AuNPs, such excess was necessary to ensure that the AuNPs were completely coated under the monolayer exchange mechanism. The nanoparticles were allowed to incubate overnight (a minimum of 12 hours). After the incubation period was complete, the AuNPs were cleaned by centrifugation at 4000 rpms and resuspension followed by sonication for 20 minutes. The clean up steps were intended to remove excess azo dye SAM from the AuNP preparation mixture.

50 nm Gold Nanoparticle Functionalization

Typically, a 100 uL volume of the 50 nm AuNP was mixed with 1 µL of either of the azo dye stock solutions ( 2 mg/mlL). As with the 2 nm AuNPs, such excess was

necessary to ensure that the AuNPs were completely coated under the monolayer exchange mechanism. The nanoparticles were allowed to incubate overnight (a minimum of 12 hours). After the incubation period was complete, the AuNPs were cleaned by centrifugation at 2500 rpms and resuspension followed by sonication for 20 minutes. The clean up steps were intended to remove excess azo dye SAM from the AuNP preparation mixture.

*Characterization of Functionalized Gold Nanoparticles*

UV-Vis Spectroscopy

Ultraviolet-Visible Spectroscopy (UV-Vis) was obtained using an Agilent 4320 Spectrophotometer (Santa Clara, CA). Samples were deposited in Quartz cuvettes (1 mm slit). Typically, 150 μL of functionalized AuNPs solution were deposited without further dilution immediately after centrifugation and resuspension of the AuNP solutions.

Transmission Electron Microscopy Imaging

Electron microscopy images were obtained using a JEOL 2010 instrument at 200 kV accelerating voltage. Samples were deposited on carbon coated (Formvar) copper grids (Ted Pella Inc. Redding, CA). Typically, a 1 μL droplet of the AuNP solution of interest was deposited on the grid, and allowed to dry at room temperature and ambient conditions. Figures 21 through 30 show the AuNP's absorption spectra and size distribution before (citrate capped AuNPs, greed data series) and after azo dye functionalization. The phenol terminated SAM data are depicted in blue series, and carboxy terminated SAM data are depicted in red series through all figures.

2 nm Gold Nanoparticles

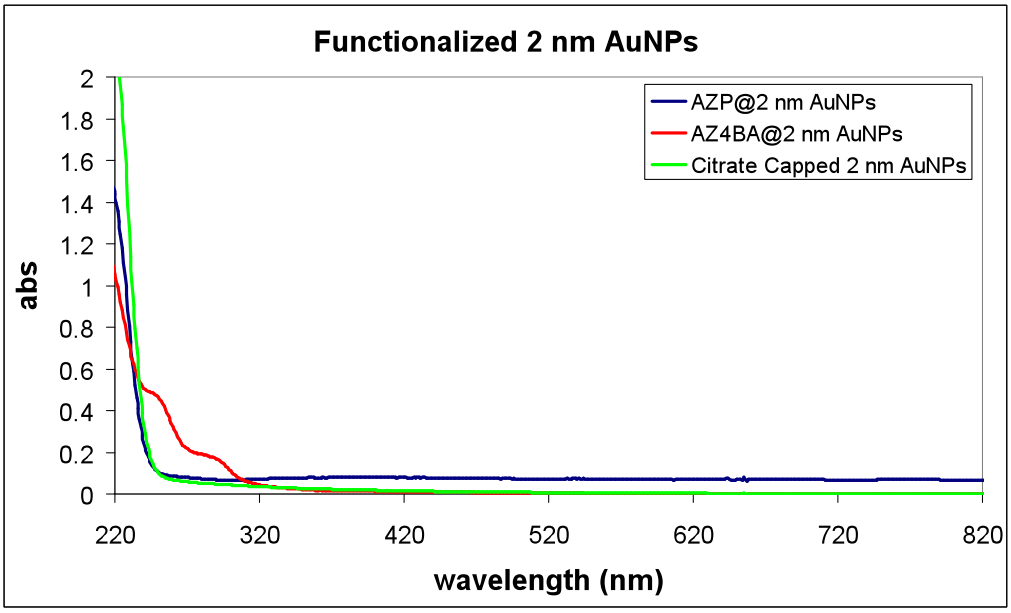


**Figure 21. UV-Vis absorption spectra of azo functionalized 2 nm AuNPs and citrate capped 2 nm AuNPs.**

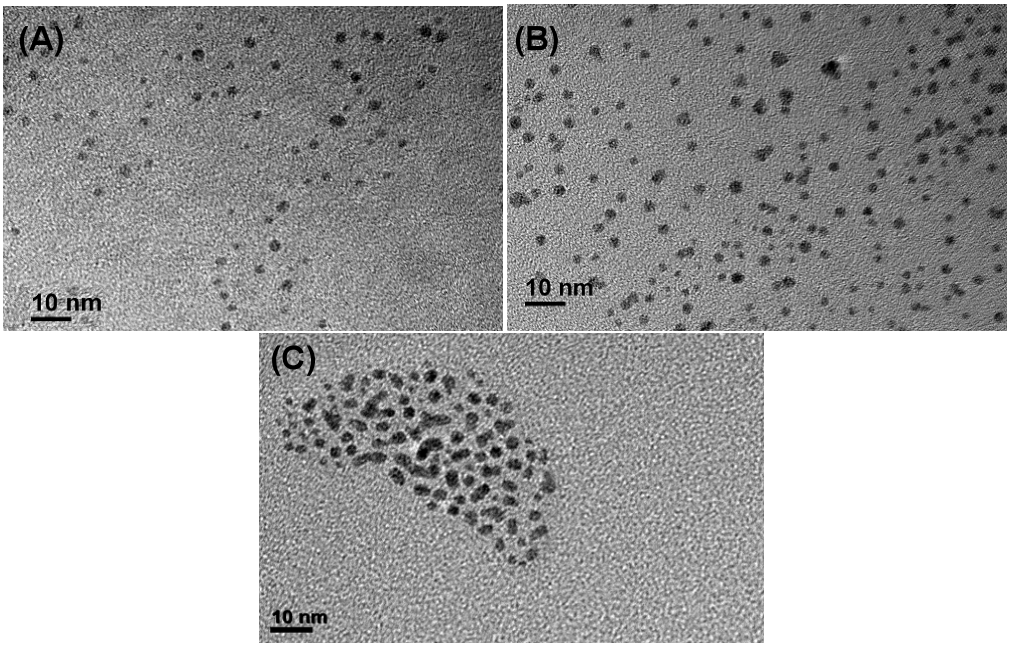


**Figure 22. TEM images of (A) AZP@2 nm AuNPs and (B) AZ4-BA@2 nm AuNPs and (C ) citrate capped 2 nm AuNPs.**

5 nm Gold Nanoparticles

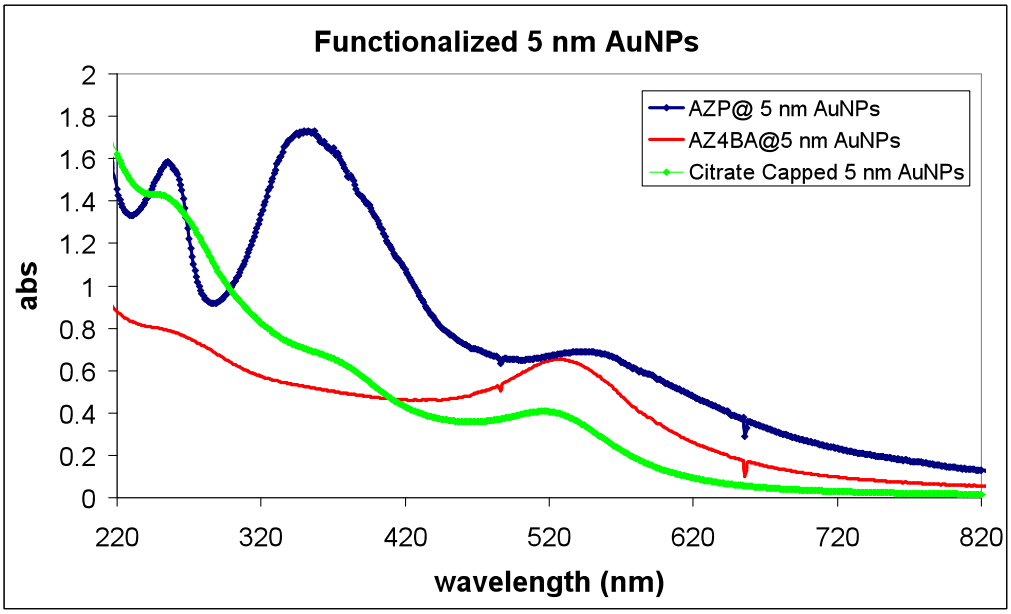


**Figure 23. UV-Vis absorption spectra of 5 nm AuNPs.**

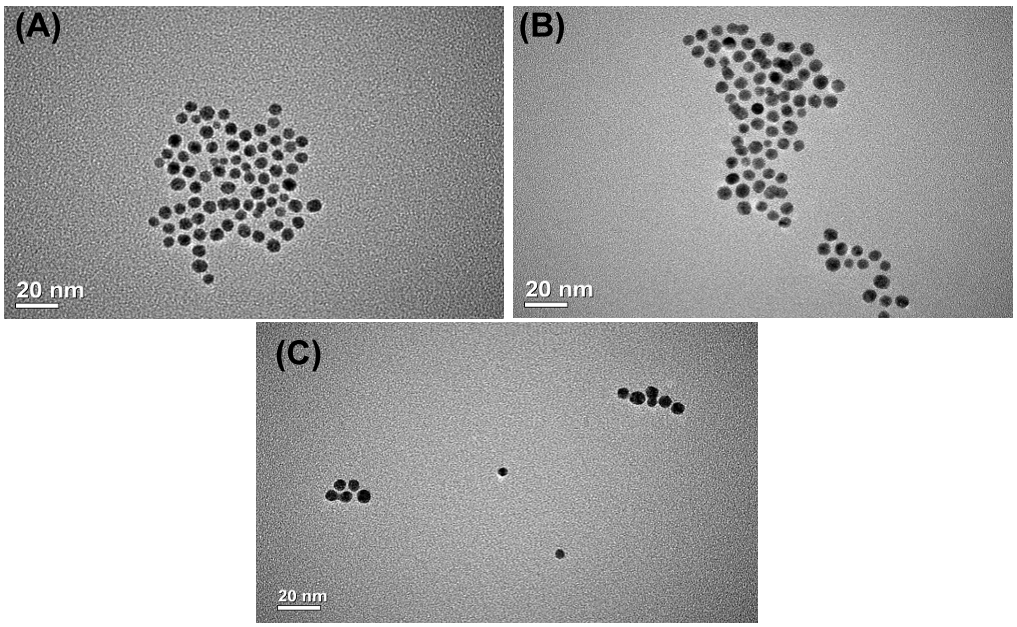


**Figure 24. TEM images of (A) AZP@5 nm AuNPs and (B) AZ4-BA@5 nm AuNPs and (C ) citrate capped 5 nm AuNPs.**

20 nm Gold Nanoparticles

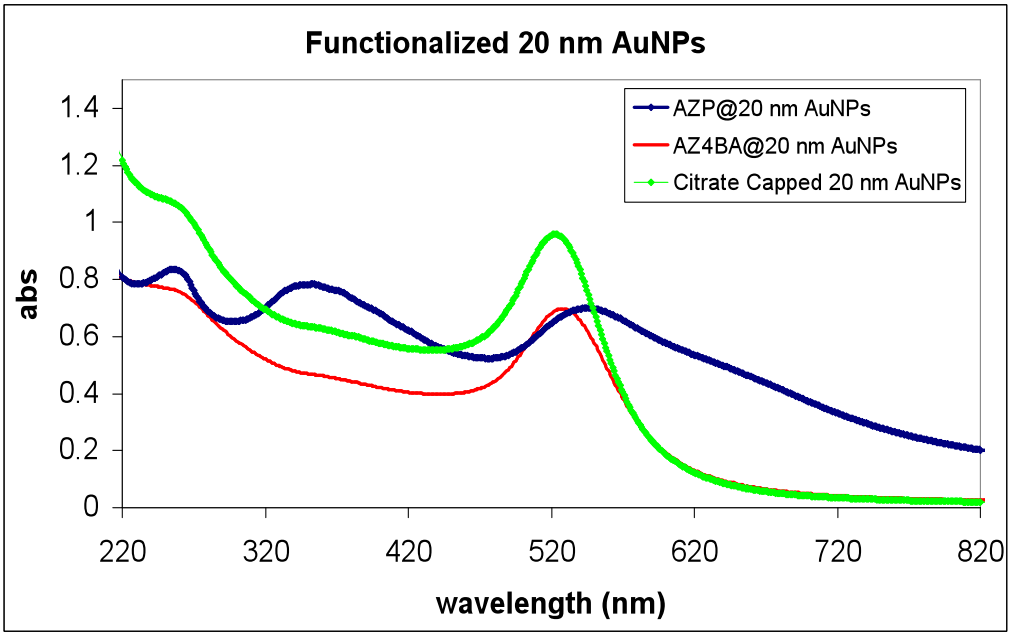


**Figure 25. UV-Vis spectra of 20 nm AuNPs.**

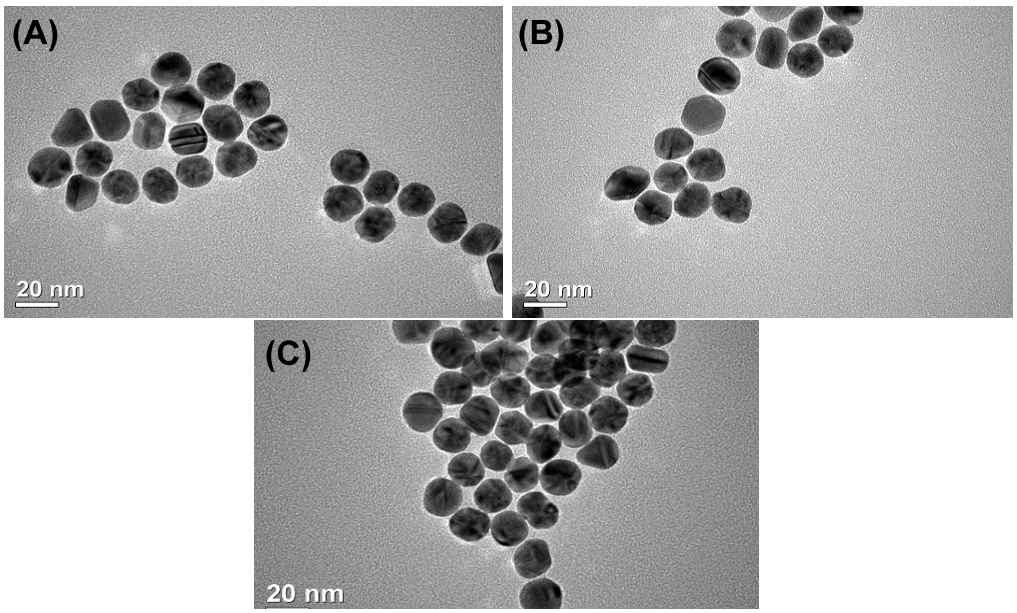


**Figure 26. TEM images of (A) AZP@20 nm AuNPs and (B) AZ4-BA@20 nm AuNPs and (C ) citrate capped 20 nm AuNPs.**

30 nm Gold Nanoparticles.

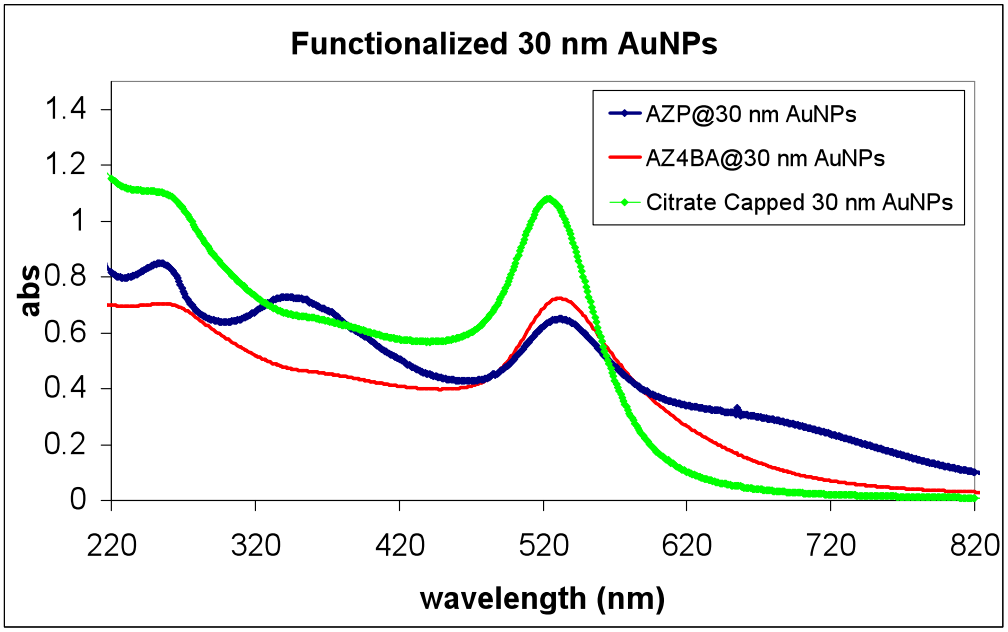


**Figure 27. UV-Vis spectra of 30 nm AuNPs.**

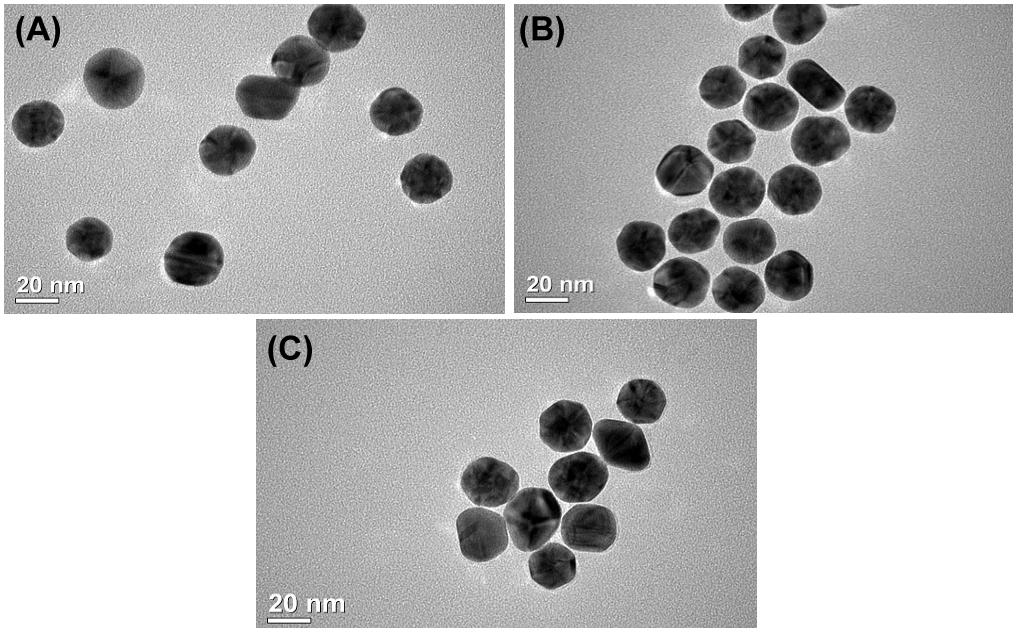


**Figure 28. TEM images of (A) AZP@30 nm AuNPs and (B) AZ4-BA@30 nm AuNPs and (C ) citrate capped 30 nm AuNPs.**

50 nm Gold Nanoparticles

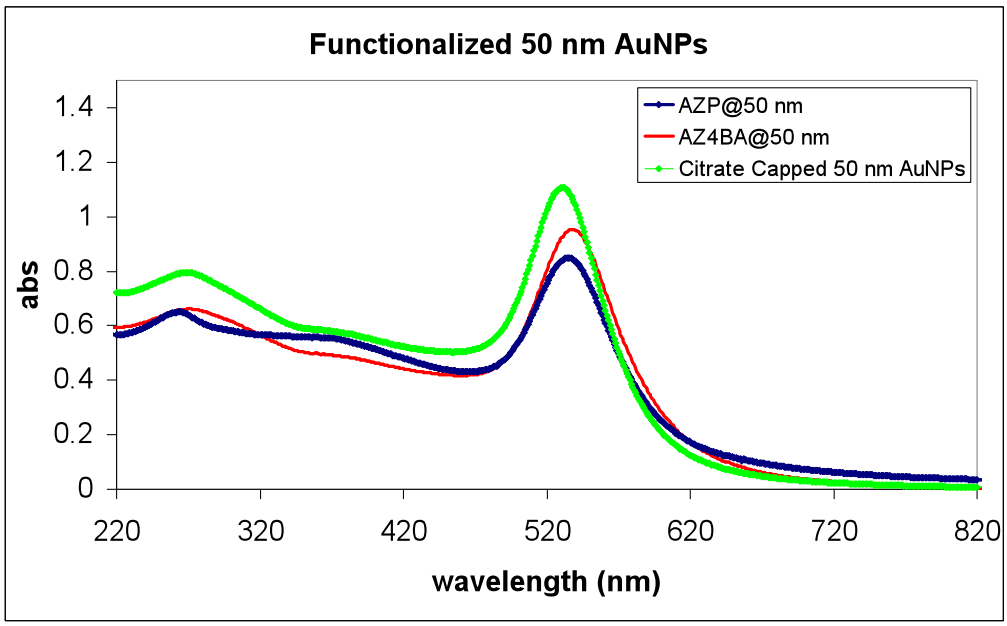


**Figure 29. UV-Vis spectra of 50 nm AuNPs.**

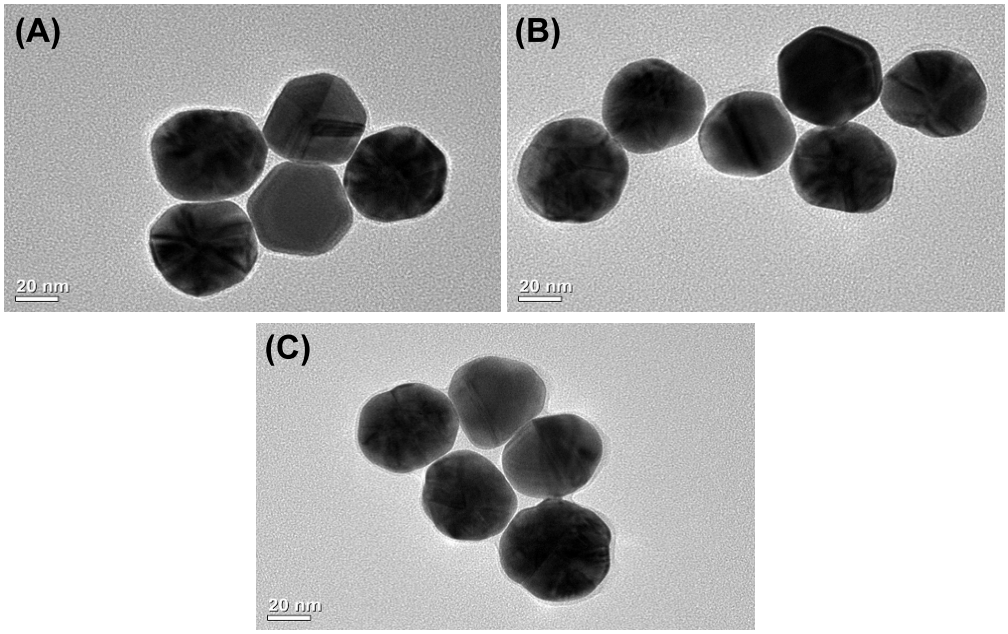


**Figure 30. TEM images of (A) AZP@50 nm AuNPs and (B) AZ4-BA@50 nm AuNPs and (C ) citrate capped 50 nm AuNPs.**

337 nm Nitrogen Laser Calibration

Laser energy measurements were taken using an Ophir Nova Power/Energy meter coupled to a PE-10 Ophir Pyroelectric head (Ophir Laser Measurement Group, North Logan, UT). Measurements were taken in increments of 50 arbitrary units on the rotatable variable neutral density filter wheel of the Voyager DE-STR (Foster City, CA). Values were recorded every 200 shots from a total of 1400 laser shots per setting point in the lower energy region (0.77 - 1.92 μJ) of the laser, and every 100 arbitrary units on the higher energy region of the laser (1.92 - 51.89 μJ). The process was repeated twice and the average calculated.

*LDI-Mass Spectrometry Experiments Using Gold Nanoparticles*

All mass spectrometry experiments were conducted on the Applied Biosystems DE-STR MALDI-TOF (Foster City, CA) instrument using a $N_2$ 337 nm Laser set up (Spectra-Physics, Irvine, CA). The applied accelerating voltage was set at 25 kV, the grid percentage was set at 65%, and delayed extraction time of 200 ns. The data was obtained using the reflectron mode on the mass spectrometer. Typically, a 15 μL aliquot of the AuNPs solution were mixed with 15 μL of the 1 mg/mLVal$^4$-Ang III (RVYVHPF) or 0.001 mM BDAC solution respectively. A 1 μL droplet was deposited on the stainless steel MALDI-MS plate. A total of 30 spots were set in the array on the MALDI-MS plate and each spot was interrogated once with 300 shots per spectrum. An average of 3 spectra was used to calculate the data points plotted in all relative ion yield comparison plots.

**Results and Discussion**

The results with azo dye capped 2, 5, 20, and 30, and 50 nm AuNPs indicate that an optimum particle size is ~5 nm. This optimum size seems to correlate to a maximum in the number of azo molecules (capping the AuNPs) per volume of AuNP solution. However, the difference in the shape of the relative ion yield patterns between the 5 nm particles and the other sizes suggest that there is also a size effect affecting the relative ion yields of the AuNPs than just the active monolayer. The 5 nm optimum size results seem to correlate to the higher ratio of absorption at approx. 340 nm than to the SPR absorption band at approx 540 nm. Because, as the size of the AuNP increases, the ratio of absorption between the 340 nm and 540 nm decreases for the AZP@AuNPs. In the other hand, at 20 and 30 nm, it is obvious that the 340 nm absorption band of the AZP@AuNP decreases with respect to the SPR band as the diameter of the AuNP increases. At 50 nm, the absorption spectra of both sets of functionalized AuNPs are dominated by the SPR band, and no absorption band is observed at 340 nm.

Results suggest that the LDI relative ion yields of the functionalized AuNPs become uniform as the absorption of both sets of functionalized AuNPs (AZP and AZ4-BA functionalized AuNPs) become similar at larger NP sizes. Such change in the optical properties of the AuNPs, *i.e.* the decrease intensity of the AZP@AuNP 340 nm absorption band with respect to the SPR band with increasing size renders the role of the SAM non-existent at large AuNP diameters. These comparative studies provide further information on the role of both, the SAM and the metallic core in the overall efficiency of the AuNP to produce ions in the LDI-MS process. At the same time, LDI-MS

experiments using BDAC as the analyte generated interesting patterns. First, the difference in relative ion yields with 2 nm AuNPs as depicted in **Fig. 31** and 5 nm AuNPs in **Fig. 32** is more dramatic than for AuNPs of larger size. Such dramatic difference in the RIY of the AuNPs can be linked to the dramatic difference in the UV-Vis spectra of the 5 nm AuNPs.

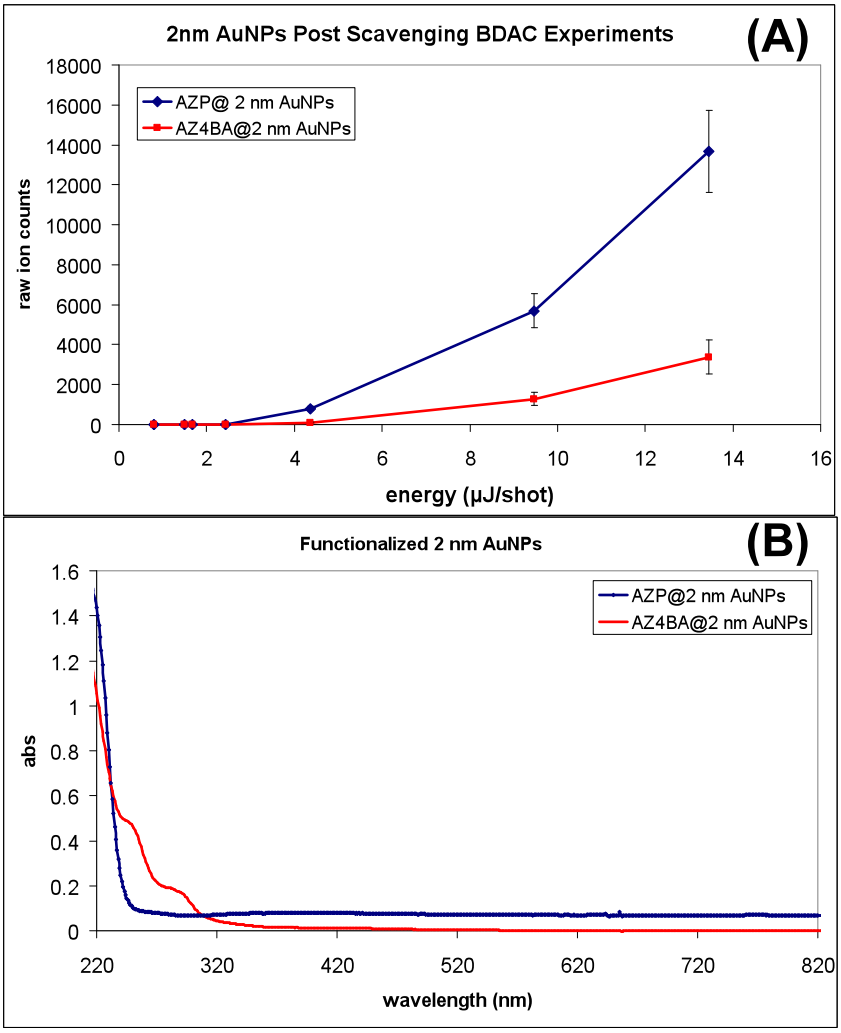


**Figure 31. (A) Relative ion yield patterns for azo functionalized 2nm AuNPs. (B) UV-Vis spectra of azo functionalized 2 nm AuNPs.**

For the 5 nm AuNPs, the AZP@AuNP has a strong absorption band at 340 nm whereas the AZ4BA@AuNP lack such absorption band. However, as the absorption band of the 5 nm AZP@AuNP is dramatically higher than the absorption band of the AZ4BA@AuNPs, the relative ion yield of the AuNPs are dramatically different. For the 2 nm AuNPs shown in **Fig. 31**, the lack of a 340 nm absorption band might be attributed to the 2 nm AuNPs being under conditions of strong quantum confinement.

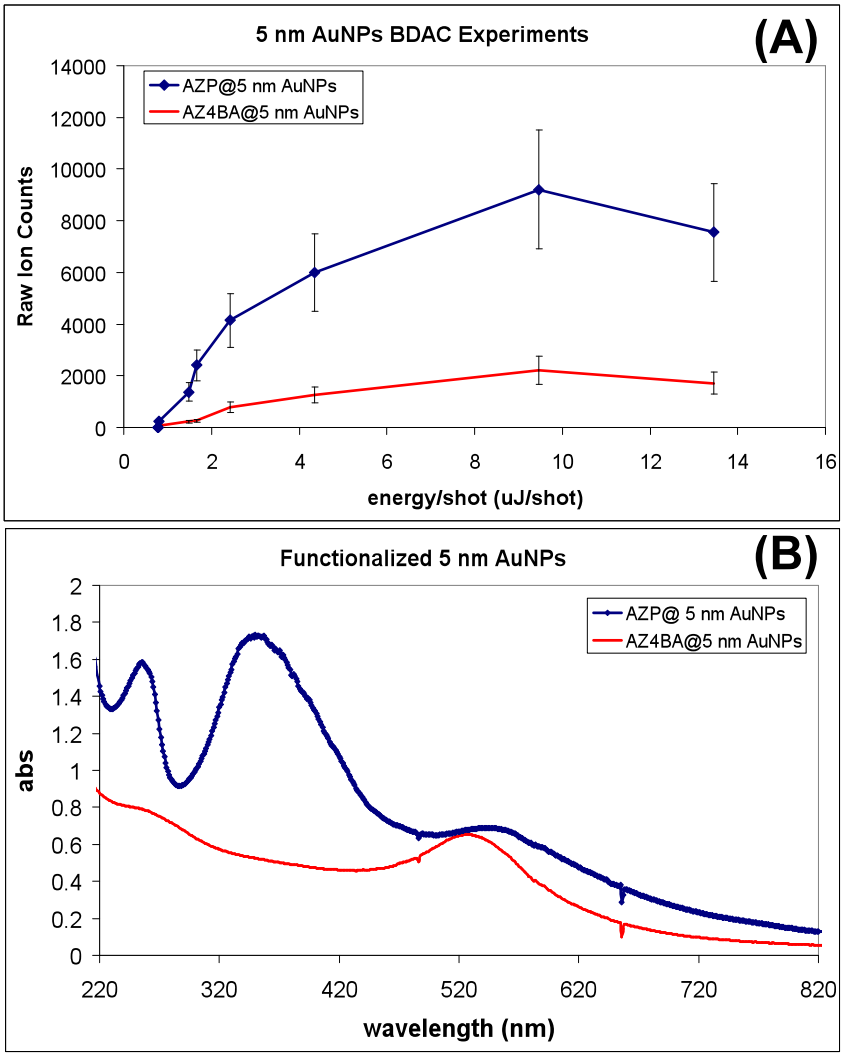


**Figure 32. (A) Relative ion yield patterns for azo functionalized 5 nm AuNPs. (B) UV-Vis spectra of azo functionalized 5 nm AuNPs.**

Therefore, with the band gap of the 2 nm AuNPs being large, the necessary electronic transitions to occur in order to have the 340 nm absorption band are not present. For the bigger AuNP sizes, as the diameter of the AuNP increases to 20, 30, and 50 nm, the intensity of the AZP@AuNP 340 nm band decreases with respect to the intensity of the SPR band at 540 nm. At the same time, the difference between the absorption spectra of the AZP@AuNP and the AZ4BA@AuNPs becomes smaller as the diameter of the AuNPs increases.

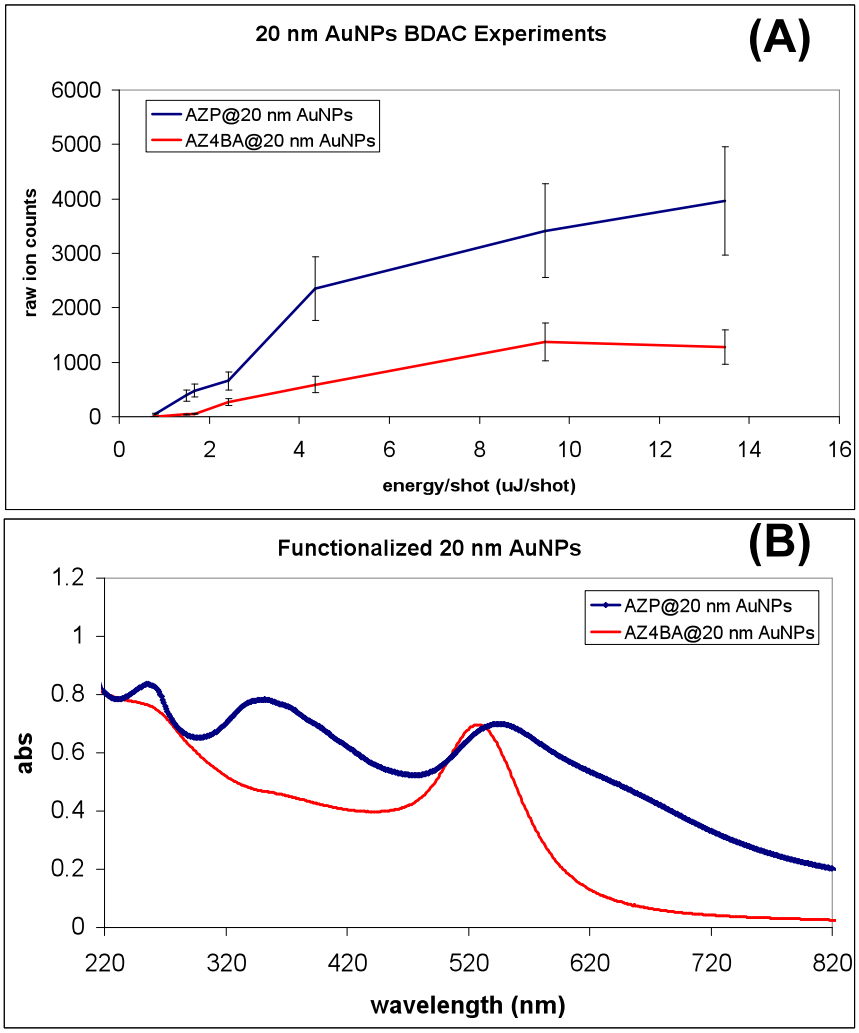


**Figure 33. (A) Relative ion yield patterns for azo functionalized 20 nm AuNPs. (B) UV-Vis spectra of azo functionalized 20 nm AuNPs.**

Therefore, the data suggests that with smaller differences in the optical spectra of both sets of functionalized AuNPs, the differences in the relative ion yields of the AuNPs become smaller. As shown in **Fig 33,** for the 20 nm AuNPs the error distribution of the AZP@AuNP and the AZ4BA@AuNP do not overlap for the BDAC experiments. But the difference in the values of the average ion counts is smaller than the differences observed for the 5 nm data set.

On the other hand, for 30 nm AuNPs shown in **Fig. 34**, as the difference in the absorption spectra is smaller, and the error distribution between the relative ion yields for the AZP@AuNP and the AZ4BA@AuNP overlap; and no significant difference is observed between both data sets. The observed behavior of the data sets can also be related to the increasingly similar absorption between both sets of the azo functionalized 30 nm AuNPs. In addition, the intensity ratios between the absorption bands at 340 nm and the SPR band at 520-530 nm become smaller as shown in **Fig 34**.

From the data, it appears that as the size of the AuNP increases, the SPR band starts to overtake the absorption spectra of the AuNPs. Therefore, as the size of the AuNPs becomes larger, the functionalized AuNPs become more metallic in nature, rendering the presence of the SAM less significant as the size of the particle increases.

Finally, for the 50 nm AuNPs, RIY of the AuNPs in the mass spectrometry data showed no significant differences in the total ion counts for the BDAC experiments. Such observation was not surprising, since the RIY of the mass spectrometry data utilizing the bigger AuNPs had become increasingly similar with bigger AuNP diameters. An additional confirmation for the observed pattern of RIY and increased

AuNP diameter was provided by the absorption spectra of the AuNP assemblies. For the AZP@AuNP, the absorption spectrum lacks the 340 nm band, making the absorption spectra of both sets of AuNPs almost equal as shown in **Fig. 35**. As the absorption spectra of both sets are similar, the relative ion yield patterns are also very similar, with no overlap of the error distribution of the data points at each energy/shot value.

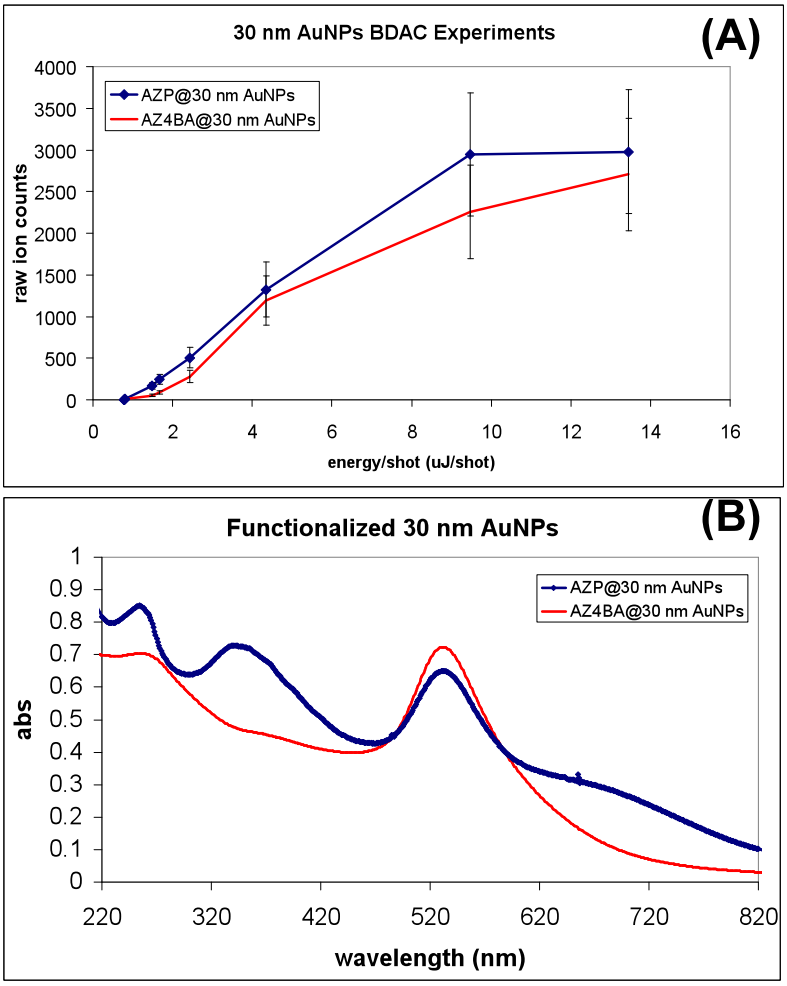


**Figure 34. (A) Relative ion yield patterns for azo functionalized 30 nm AuNPs. (B) UV-Vis spectra of azo functionalized 30 nm AuNPs.**

Overall, the data then suggests that as the size of the AuNP increases, the contribution of the SAM to the overall process disappears.

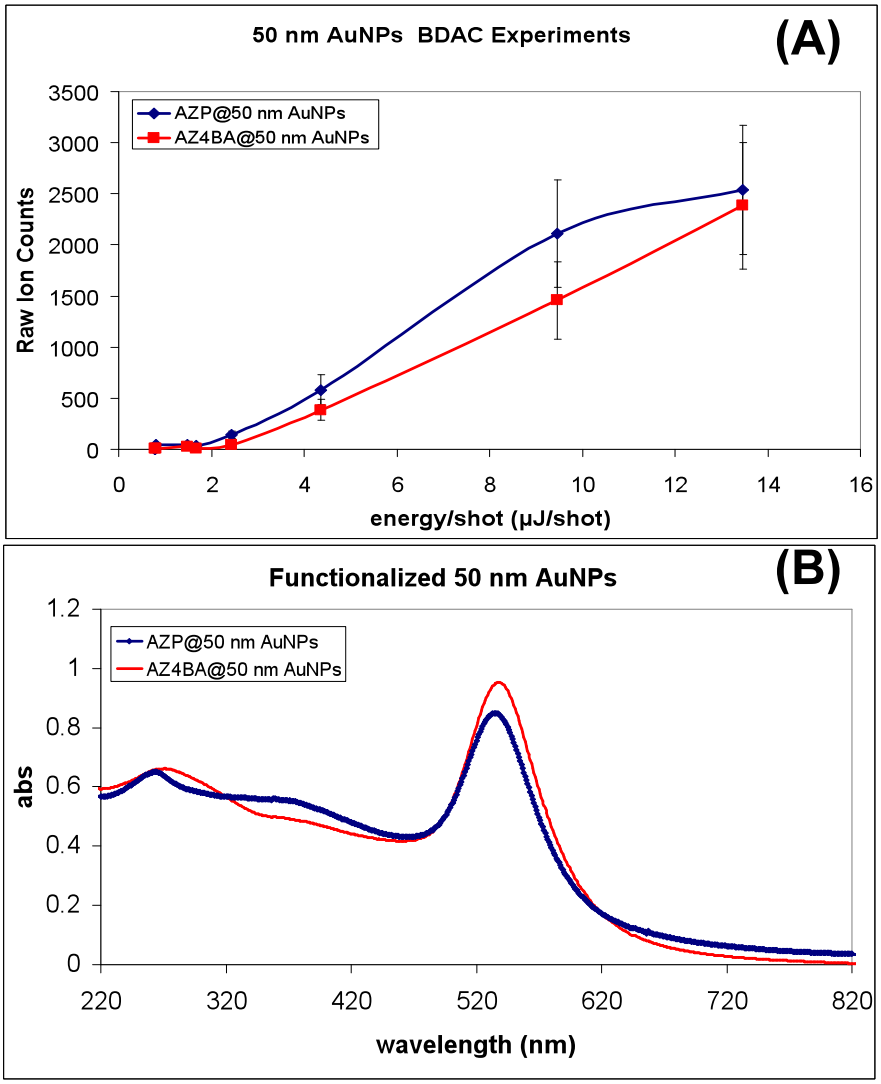


**Figure 35. (A) Relative ion yield patterns for azo functionalized 50 nm AuNPs. (B) UV-Vis spectra of azo functionalized 50 nm AuNPs.**

Our data also suggests that the photophysical properties of the SAM on the AuNP and the subsequent energy deposition role of the SAM are "turned off" as the AuNP becomes larger. As the contribution of the SAM diminishes, the character of the

functionalized AuNP becomes more similar to the "bare AuNPs", and making the SAM a mere spectator in the LDI process regardless of the electron donating/withdrawing nature of the functional groups. The data also demonstrates that the optical properties of the functionalized AuNPs directly affect the relative ion yield of the AuNPs. That is, the AuNPs that have a higher absorbance at approx. 337 nm generate higher relative ion yields than the AuNPs that show low absorbance at approx. 337 nm.

The patterns of the relative ion yields between the functionalized AuNPs become more uniform as the size of the AuNP increases. The observed phenomena might be attributed to the decrease in the relative layer thickness of the SAM in relation to the increasing core size. The change in core size then alters the amount and efficiency of energy transfer by the SAM in the LDI process, as the metallic core conducts most of the energy deposition. However, the patterns in relative ion yield remain in spite of the nature of the analyte, as the experiments were also conducted using $Val^4$-Angiotensin III (RVYVHPF) as the analyte.

For the BDAC experiments, the quaternary amine nature of the BDAC surfactant ruled out the protonation step for ionization. By ruling out the need for proton transfer in the ionization event, we eliminate the role of the functional group on the SAM. Thus, the switch of analyte allowed the focus of the analysis to center on the energy deposition capabilities of the AuNPs; without having to take into account the molecular characteristics of the SAM, but only the overall optical and photophysical qualities of the functionalized AuNPs.

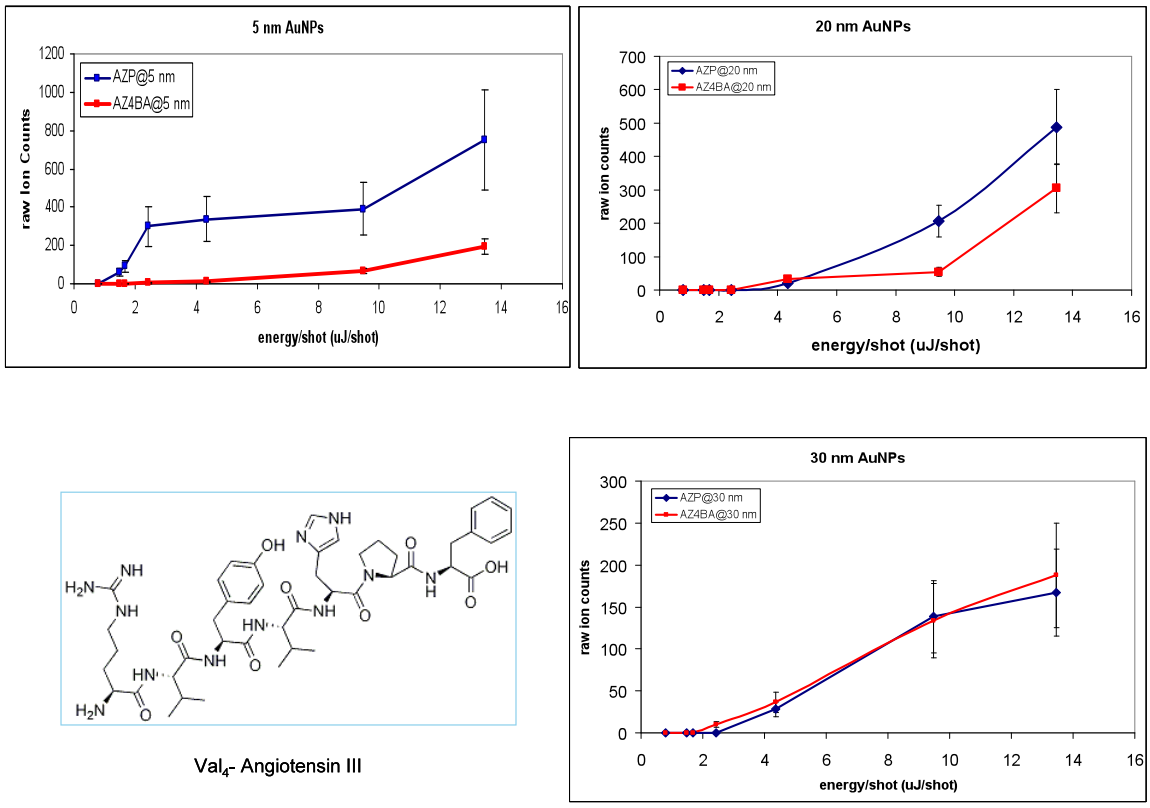


**Figure 36. Relative ion yield patterns for AZP@AuNPs and AZ-4BA@ AuNPs.**

For the experiments using Val$^4$-Angiotensin III (RVYVHPF), consistent with the BDAC experiments, the most dramatic difference between the relative ion yields of both the AZP@AuNPs and the AZ4BA@AuNPs were observed with 5 nm AuNPs as shown in **Fig. 36**. Such fact is not surprising as the absorption spectra of the 5 nm AuNPs are very different between both sets of functionalized AuNPs. For 20 nm AuNPs, the patterns between the AZP and AZ4BA coated AuNPs started to become more uniform, but there was some difference between the error distributions of both sets. For 30 nm AuNPs, difference between the patterns of relative ion yields disappeared, and both sets of data completely overlapped with each other. It is important to note that as the size of

the AuNP increases, the total number of maximum ion counts decreases, in both, the BDAC and Val$^4$-Angiotensin III experiments. For instance, the maximum ion counts observed for 5 nm AuNPs with BDAC was approx 10,000 counts; on the other hand, for 50 nm AuNPs using BDAC, the maximum amount of ion counts is approx. 2500 counts. Similarly, for 5 nm AuNPs using Val$^4$-Angiontensin III (RVYVHPF), the maximum amount of ion counts is approx. 1000 counts, whereas for 30 nm AuNPs, the maximum amount of ion counts was approx. 250.

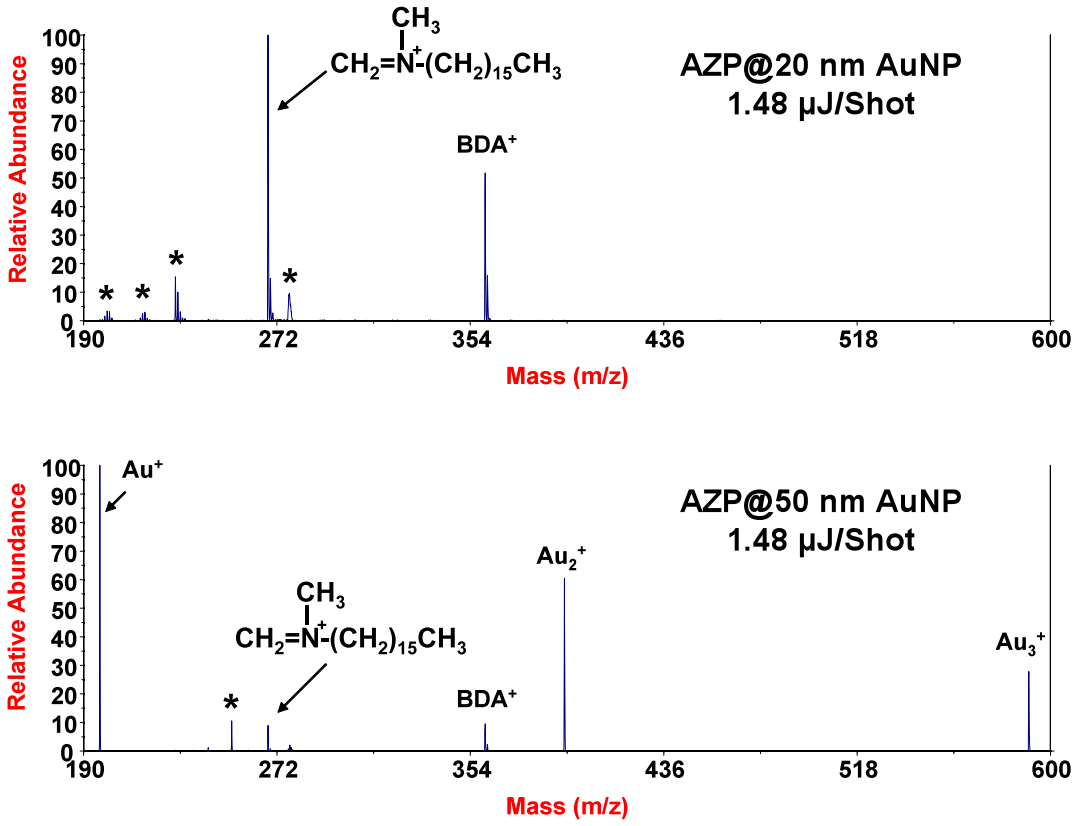


**Figure 37. Mass spectra comparison of ion signal intensity of gold clusters vs analyte ion at 1.48 µJ/shot for 20 nm AZP@20 nm AuNPs and AZP@50 nm AuNPs.**

It is interesting to see that there was no $[M+H]^+$ signal observed for 50 nm AuNPs for the $Val^4$-Angiotensin III (RVYVHPF) experiments with either set of functionalized AuNPs. It is also important to note that the 2 nm AuNPs did not generate $[M+H]^+$ signal for the peptide experiments at the energy settings used in our analysis. Another important aspect in analyzing the effect of AuNP size on the relative ion yield of the gold nanoparticles is the presence of gold clusters in the mass spectrometry data. By comparing the abundance of the gold clusters against the abundance of the analyte ion signal, it becomes possible to learn which nanoparticle size is the most efficient in producing analyte ions and not gold clusters as shown in **Fig 37**. Such ratios serve as indicators of the capacity of the AuNP to conduct energy deposition to the analyte without forming gold clusters, hence, transmitting the energy from the particle to the analyte more efficiently.

For the BDAC experiments, at low laser energies per shot, there are no gold cluster ion signals for the 5 and 20 nm AuNPs as shown in **Fig. 38**. On the other hand, for 30 nm, the analyte signal dominates the spectra, but the gold clusters have a significant presence in the mass spectra. As for the 50 nm AuNPs, the mass spectra are dominated by gold clusters. The observed pattern shows that as the size of the AuNP increases, the amount of gold clusters increase significantly. It is interesting to point out that for the 2 nm AuNPs, there is no detectable signal in the mass spectra at low laser energies. For the 2 nm AuNPs, signals start to appear up until very high laser energies/shot values are applied.

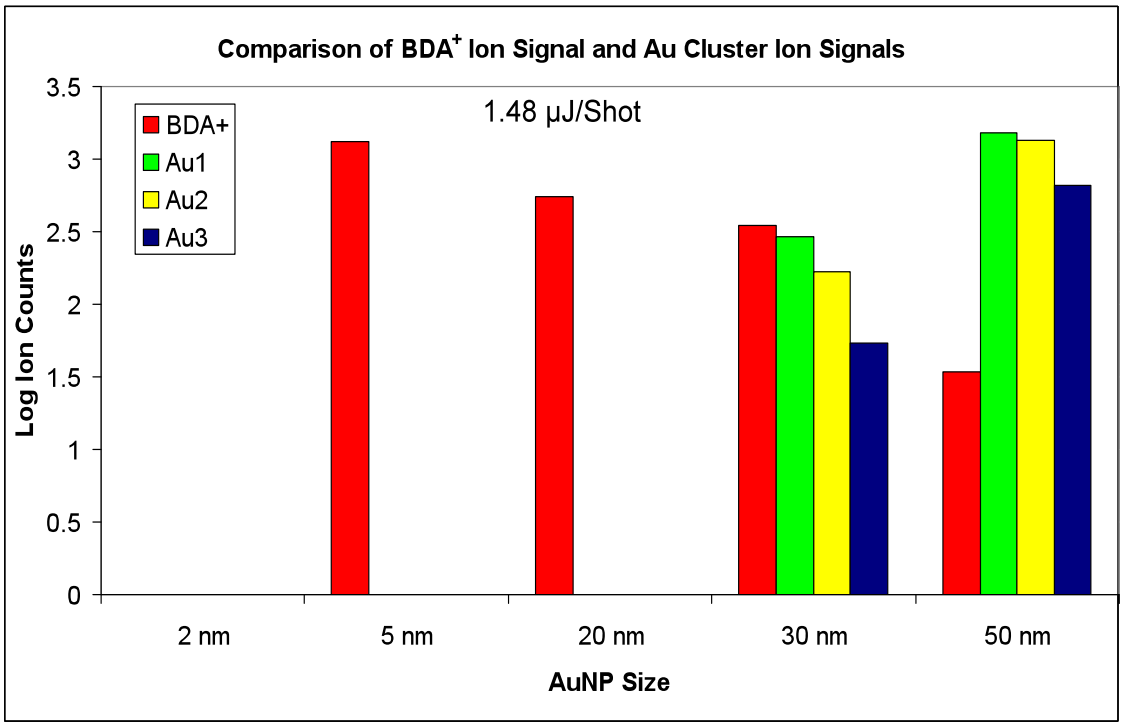


**Figure 38. Bar chart comparing the abundances of $BDA^+$ ion signal vs gold cluster ion signals at µJ/shot 1.48 µJ/shot.**

At higher laser energy/shot settings, the ratio of analyte ion signal vs Au cluster signals show some interesting patterns. As shown in **Fig 39**, for the 2 nm AuNPs, the spectra are dominated by the analyte signal, whereas the 5 nm AuNPs the mass spectra have no Au clusters signals. On the other hand, at 20, 30 and 50 nm AuNPs, the Au cluster signals become more abundant as the size of the AuNP increases. This trend continues to the point where the mass spectra became dominated by the Au clusters at 30 and 50 nm diameters. It is interesting to observe that the pattern of gold cluster vs analyte ion signal also applies to experiments using the $Val^4$-Ang III (RVYVHPF) as analyte.

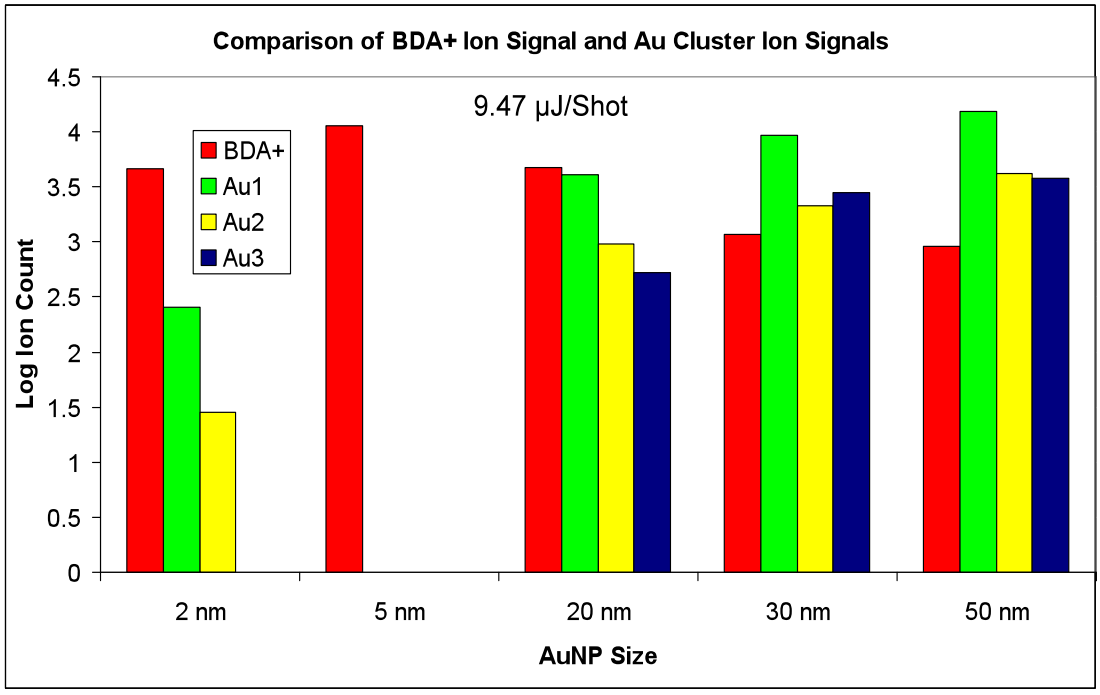


**Figure 39. Bar chart comparing the abundances of $BDA^+$ ion signal vs gold cluster ion signals at µJ/shot 9.47 µJ/shot.**

At low energy/shot settings, the spectra show no gold clusters for the 5 nm AuNPs as shown in **Fig. 40**. For the 20, 30, and 50 nm, the mass spectra are dominated by gold clusters with no analyte signal present at low energies. However, when the energy was increased to 9.47 µJ/shot, the amount of gold clusters become the dominant ion signals for 20, 30, and 50 nm AuNPs as shown in **Fig 41.** It is highly interesting that at 5 nm AuNPs, there are no gold clusters observed in the mass spectra, both at 1.47 and 9.48 µJ/shot. It is also interesting to see that at high energies, the 2 nm AuNPs generated no detectable ion signals for the analyte peak, or for the gold clusters. For the 2nm AuNPs, very low signals were observed only at high energy/shot settings above 25 µJ/shot.

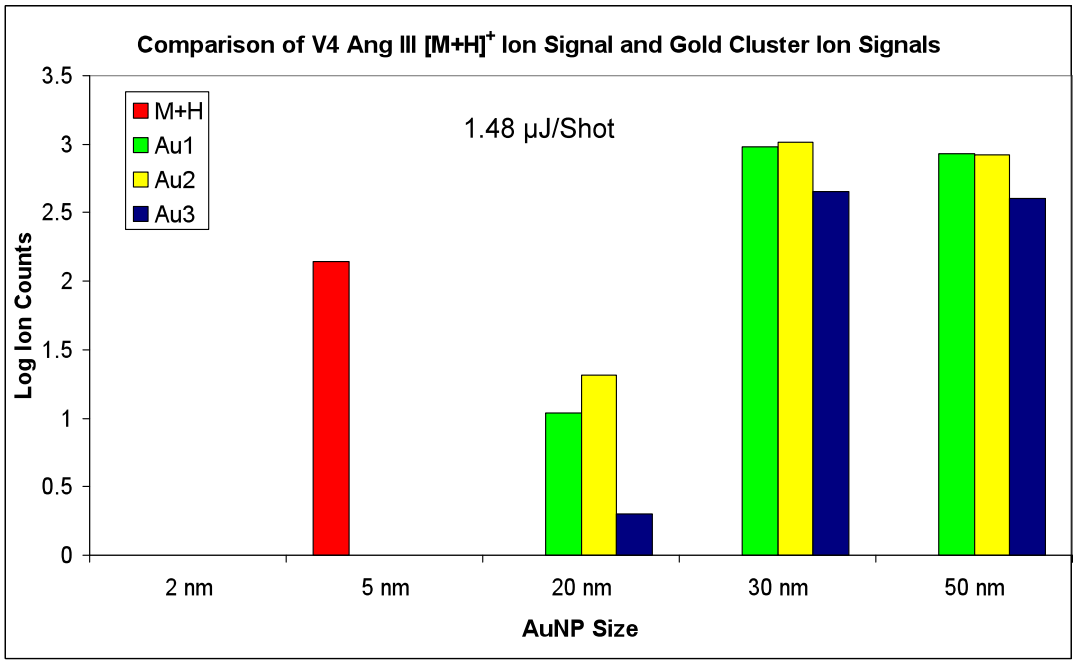


**Figure 40. Bar chart comparing Val$^4$-Angiotensin III $[M+H]^+$ ion signal vs gold clusters ion signals at 1.48 µJ/shot.**

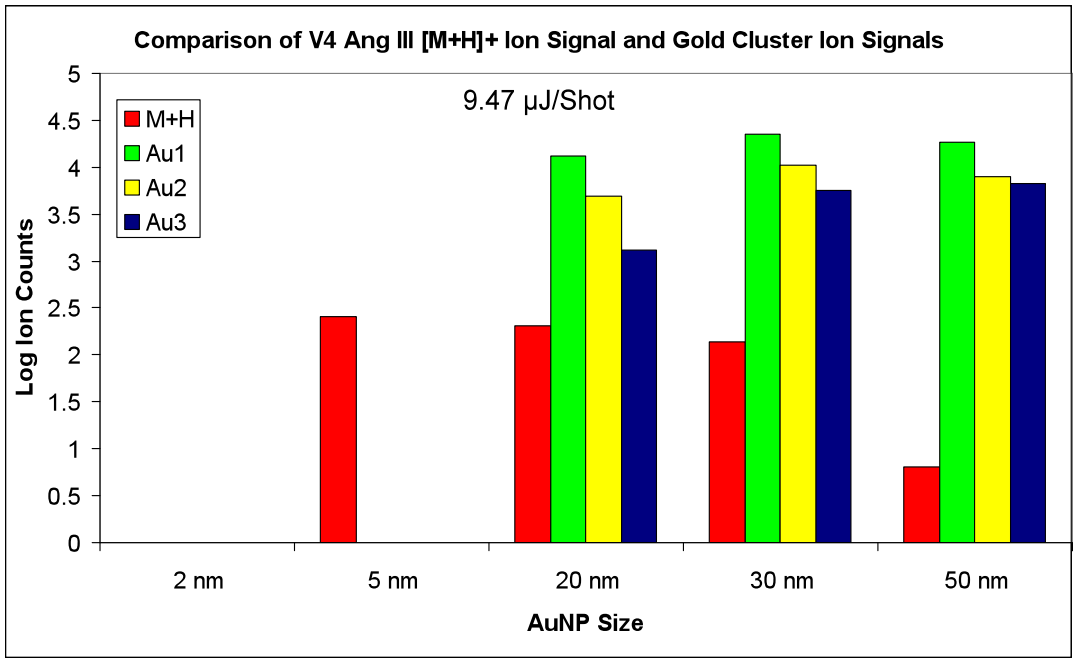


**Figure 41. Bar chart comparing Val$^4$-Angiotensin III $[M+H]^+$ ion signal vs gold Clusters ion signals at 9.47 µJ/shot.**

Our results illustrate that the functionalized 5 nm AuNP were the most efficient AuNPs size to produce ion signals for both types of analytes. The results also support the postulate that as the size of the AuNP increases, the role of the SAM to conduct energy deposition decreases, to the point that the LDI process is driven by the metallic core, and thus, more gold clusters are obtained in the LDI data. Such phenomena might be attributed to the fact that 5 nm AuNPs are the best combination of SAM thickness to core diameter ratio, and the highest amount of SAM on the AuNP per unit volume.

It is also important to note that 2, 5 and 20 nm AuNPs fall within the intrinsic size effect, where as 30 and 50 nm AuNPs fall in the extrinsic size effect. Both, the intrinsic and extrinsic size effect regimes have different photophysical characteristics. Therefore, it is not surprising to see that such differences in the optical properties of the AuNPs alter their efficiency and behavior in LDI experiments. However, as the 2 nm AuNPs are under strong quantum confinement conditions, the energy distribution of such small particles is highly different than the AuNPs that are not under quantum confinement. Thus, the capacity of the 2 nm AuNPs to transfer energy is limited causing the ion counts using the 2 nm AuNPs to be non existent for the peptide experiments, or as shown in our data, lower than the 5 nm counterparts for the BDAC experiments.

**Summary**

The AuNP size effect experiments provide valuable information on the role of both, the SAM and the metallic core of the AuNP. The data suggests that the optimal size for the most efficient use of the SAM is 5 nm. That is, when functionalizing AuNPs for practical applications geared to mass spectrometry experiments, the effect of the

presence of the SAM will be at its highest affectivity with the 5 nm AuNPs. In addition, as the size of the AuNP increases, the photophysical properties of the AuNPs become more uniform between functionalized AuNPs sets.

Our data demonstrates that as the diameter of the AuNP increases, the SPR band becomes the prominent feature in the AuNP absorption spectra, and thus, the process to transfer energy from the laser irradiation to the analyte becomes increasingly dependant on the metallic core, and not the sum of the metallic core and the SAM. As the larger metallic core overtakes the energy deposition process, the mass spectra are dominated by gold clusters, thus diminishing the ability of the AuNPs to generate analyte ions.

# CHAPTER IV

# CONCLUSIONS

To fully exploit AuNPs for LDI-MS applications, a through understanding of the behavior of the SAM and the gold core is necessary. The experimental results in this document provide valuable information regarding the effect of changes in surface chemistry and nanoparticle size on the photophysical properties of AuNPs. Our studies have demonstrated that subtle changes in the molecular frame of the SAM alter the capacity of the AuNPs to generate analyte ion signals under LDI. The results with $Val^4$-Angiotensin III (RVYVHPF) and BDAC demonstrated that turning off the (-N=N-) chromophore, decreased the capacity of the AuNP to generate analyte ions. In addition, changes in the terminal functional group of the SAM were also shown to alter the photophysical properties of the AuNPs, affecting their capacity to generate analyte ions under LDI experimental conditions, and thus validating our hypothesis, that the presence of an active chromophore serving as a SAM enhances the ionization efficiency of the AuNPs.

Additionally, changes in the diameter of the AuNPs were shown to directly affect the relative ion yields of the AuNPs as a consequence of strong changes in the photophysical properties of the AuNPs. To that end, the ionization patterns between the AZP@AuNPs and AZ4BA@AuNPs have been shown to become increasingly similar between AuNP sets, as the AuNPs lose the strong optical absorption at approx 340 nm with increasing AuNP sizes. Our studies on the relative ion yield of the azo SAM to produce analyte ion signals led to an investigation on the statistical relationships

between the abundance of analyte ions versus gold cluster ion signals. The variations in the abundance of gold clusters in the LDI-MS data suggest that the bigger nanoparticles are less efficient in transferring energy to the analyte. Such observation is supported by the fact that 5nm AuNPs generated mass spectrometry data lacking the presence of gold clusters for both sets of experiments, the $Val^4$-Angiotensin III (RVYVHPF) and BDAC studies.

On the other hand, the 50 nm AuNPs generated mass spectrometry data that was dominated by the atomic ion of gold and gold clusters ($Au_2^+$ and $Au_3^+$) with very low amounts of analyte ion signal for the BDAC experiments, and not $[M+H]^+$ signal for the $Val^4$-Angiontensin III (RVYVHPF) experiments. Therefore, our studies have validated our hypothesis that as the size of the AuNP increases, the role of the SAM to enhance energy deposition to the analyte decreases significantly. Thus, our experiments provide insight into the photophysical mechanisms of gold nanoparticles as LDI platforms.

Considering that AuNP research geared to mass spectrometry applications is gaining widespread popularity in chemical research around the world, deep understanding of the physical dynamics behind AuNPs is necessary. Future experiments could include the study of variations in RIY under different laser irradiations, for example 532 nm in order to explore the behavior of the AuNPs with excitation wavelengths close to the SPR band. In addition, the AuNPs could also be subjected to photoswitching experiments exploring the effect of changing the SAM from the *trans* to *cis* conformations, and studying the RIY patterns for both conformation on the AuNPs surface.

In addition, the role of the AuNP could also be explored by conducting experiments using non-metallic AuNPs such as silicon based nanoparticles. Such studies could provide valuable insight into the fundamental principles behind AuNPs dynamics by altering the nature of the nanoparticle core into non-metallic particles coated with azo dyes. Studies could also explore the use of increasing silicon nanoparticle sizes, from 7 to 40 nm particles. However, such studies require pre-functionalization of the silica particles with silane linkers, thus, such studies would require method development.

Finally, gold nanoparticles constitute a versatile chemical platform that provides a wide array of potential applications for mass spectrometry. We have demonstrated that the key aspect in exploiting the benefits of AuNPs for mass spectrometry applications is the maximization of the role of the SAM once it is bound to the AuNP surface. Such maximization of the impact of the SAM can only be achieved by selecting the right combination of particle diameter, and molecular characteristics of the SAM bound to the surface of the AuNPs. As our data demonstrated, changes in the molecular structure of the SAM, as well as changes in the diameter of the AuNP directly affect the RIY of the AuNPs under LDI experiments.

REFERENCES


1. Yates, J. *Journal of Mass Spectrometry* **1998,** *33*, 1-19.

2. Eustis, S.; El-Sayed, A. *Chem. Soc. Rev.* **2006**, *35*, 209-217.

3. Xiao, Y.; Patolsky, F.; Katz, E.; Hainfeld, J. F.; Willner, I. *Science* **2003**, *299*, 1877-1881.

4. Nam, J.-M.; Thaxton, C. S.; Mirkin, C. A. *Science* **2003**, *301*, 1884-1886.

5. Mulvaney, S. P.; Musick, M. D.; Keating, C. D.; Natan, M. J. *Langmuir* **2003**, *19*, 4784-4790.

6. Penn, S. G.; He, L.; Natan, M. J. *Curr. Opin. Chem. Biol*. **2003**, *7*, 609-615.

7. Tanaka, K.; Waki, H.; Ido, Y.; Akita, S.; Yoshida, Y.; Yoshida, T. *Rapid Commun. Mass. Spectrom*. **1988**, *2*, 151-153.

8. Karas, M.; Hillenkamp, F. *Anal. Chem.* **1988**, *60*, 2299-2301.

9. Strupat, K.; Karas, M.; Hillenkamp, F. *Int. J. Mass Spectrom. Ion Proc.* **1991**, *111*, 89-102.

10. Fitzgerald, M. C.; Parr, G. R.; Smith, L. M. *Anal. Chem.* **1993**, *65*, 3204-3211.

11. Vorm, O.; Roepstorff, P.; Mann, M. *Anal. Chem.* **1994**, *66*, 3281-3287.

12. Westman, A.; Huth-Fehre, T.; Demirev, P.; Sundqvist, B. U. R. *J. Mass Spectrom.* **1995**, *30*, 206-211.

13. Gusev, A. I.; Wilkinson, W. R.; Proctor, A.; Hercules, D. M. *Anal. Chem.* **1995**, *67*, 1034-1041.

14. Dai, Y.; Whittal, R. M.; Li, L. *Anal. Chem.* **1996**, *68*, 2494-2500.

15. Amado, F. M. L.; Domingues, P.; Graça Santana-Marques, M.; Ferrer-Correia, A. J.; Tomer, K. B. *Rapid Comm. Mass Spectrom.* **1997**, *11*, 1347-1352.

16. Figueroa, I. D.; Torres, O.; Russell, D. H. *Anal. Chem.* **1998**, *70*, 4527-4533.

17. Dale, M. J.; Knochenmuss, R.; Zenobi, R. *Anal. Chem.* **1996**, *68*, 3321-3329.

18. Schurenberg, M.; Dreisewerd, K.; Hillenkamp, F. *Anal. Chem.* **1999**, *71*, 221-229.

19. Wei, J.; Buriak, J. M.; Siuzdak, G. *Nature* **1999**, *399*, 243-246.

20. Go, E. P.; Apon, J. V.; Luo, G.; Saghatelian, A.; Daniels, R. H.; Sahi, V.; Dubrow, R.; Cravatt, B. F.; Vertes, A.; Siuzdak, G. *Anal. Chem.* **2005**, *77*, 1641-1646.

21. Finkel, N. H.; Prevo, B. G.; Velev, O. D.; He, L. *Anal. Chem.* **2005**, *77*, 1088-1095.

22. Kauppila, T. J.; Talaty, N.; Salo, P. K.; Kotiaho, T.; Kostiainen, R.; Cooks, R. G. *Rapid Comm. Mass Spectrom.* **2006**, *20*, 2143-2150.

23. Chen, Y.; Vertes, A. *Anal. Chem.* **2006**, *78*, 5835-5844.

24. Wen, X.; Dagan, S.; Wysocki, V. H. *Anal. Chem.* **2007**, *79*, 434-444.

25. Chen, Y.; Luo, G.; Diao, J.; Chornoguz, O.; Reeves, M.; Vertes, A. *J. Phys.: Conf. Series* **2007**, *59*, 548-554.

26. Guo, Z.; Ganawi, A.; Liu, Q.; He, L. *Anal. Bioanal. Chem.* **2006,** *384*, 584-592.

27. Teng, C. H.; Ho, K. C.; Lin, Y.S.; Chen, Y.-C. *Anal. Chem*. **2004**, *76*, 4337-4342.

28. McLean, J. A.; Stumpo, K. A.; Russell, D. H. *J. Am. Chem. Soc.* **2005**, *127*, 5304-5305.

29. Castellana, E. T.; Russell, D. H. *Nano Lett.* **2007**, *7*, 3023-3025.

30. Stumpo, K.A.; Russell, D.H.; *J. Phys. Chem. C.* **2009**, *113*, (5), 1641-1647.

31. Castellana, E.T.; Gamez, R.C.; Gomez, M.E.; Russell, D.H. *Langmuir*, **2010**, *26*, (8), 6066-6070.

32. Battistini, G.; Cozzi, P.G..; Jalkanen, J.P.; Montalti, M.; Prodi, L.; Zaccheroni, N.; Zerbetto, F. *ACS Nano*. **2008**, *2*, 1, 77-84.

33. Lin, Y.; Yu, B.; Lin, W.; Lee, S.; Kuo, C.; Shyue, J. *Journal of Colloid and Interface Science*. **2009**, *340*, 126-130.

34. Juhasz, P.; Costellow, C. E.; Biemann, K. *J. Am. Soc. Mass. Spectrom.* **1993**, *4,* 399-409.

35. Briquet, L.; Vercauteren, D. P.; André, J. M.; Perpète, E. A.; Jacquemin, D. *Chemical Physics Letters* **2007**, *435* (4-6), 257-262.

36. Manna, A.; Peng-Lei, Chen, P.; Akiyama, H.; Wei, T.; Tamada, K.; Knoll, W. *Chemistry of Materials.* **2003**, *15*, (1), 20-28.

37. Ohlsson, J.; Wolpher, A.; Hagfeldt, A.; Grennberg, H. *Journal of Photochemistry and Photobiology A*, **2002**, *148*, 41-48.

38. Chang-Rui, Z. and Yu-Lu, W. *Synthetic Communications*. **2003**, *33*, 24, 4205-4208.

39. Link, S.; El-Sayed, M. *J. Phys. Chem. B.* **1999**, *103*, 8410-8426.

40. Rao, C. N. R.; Kulkarni, G.U.; Thomas P.;J.; Edwards, P.P. *Chem. Eur. J.* **2002**, *8*, 1, 28-35.

41. Link, S.; El-Sayed, M. *J. Phys. Chem. B*. **1999**, *103*, 4212-4217.

42. Kelly, K.L.; Coronado, E.; Zhao, L. L.; Schatz,G.C.; *J. Phys. Chem. B*. **2003**, *107*, 668-677

# VITA

Mario Estuardo Gomez Hernandez was born in Guatemala City. He received a Bachelor of Science degree in chemistry from Texas A&M-University-Kingsville in 2003. He also received a Master of Science degree in organic chemistry from Texas A&M University-Kingsville in 2006. In the fall of 2006, Mario joined the Russell Research Laboratory at Texas A&M University to study mass spectrometry and gold nanoparticles, earning a Master of Science Degree in May 2011. Mario has received awards from the First Year Chemistry Teaching program at Texas A&M University. He is a certified JEOL 2010 Transmission Electron Microscopy user for High Resolution TEM by the Microscopy and Imaging Center at Texas A&M University. He may be reached at the department of Atmospheric Sciences at Texas A&M University at 1204 Eller O&M Building room 1109E in College Station, TX. 77840. His current email address is mgomez@mail.chem.tamu.edu